

Supplementary Information

Vince Buffalo and Graham Coop

Contents

| | |
|---|-----------|
| S1 Estimator Bias Correction | 2 |
| S1.1 Correcting variance bias with a single depth sampling process | 2 |
| S1.2 Correcting variance bias with individual and depth sampling processes | 3 |
| S1.3 Covariance Correction | 4 |
| S1.4 Temporal-Replicate Covariance Matrix Correction | 5 |
| S2 Barghi et al. (2019) Temporal Covariances | 6 |
| S3 Block Bootstrap Procedure | 6 |
| S4 Replicate $G(t)$ and Partitioning the Variance in Allele Frequency | 7 |
| S5 The Empirical Neutral Null Windowed Covariance Distribution | 9 |
| S6 Bergland et al. (2014) Re-Analysis | 9 |
| S7 Approximating the Reduction in Diversity from $G(t)$ | 12 |
| S8 Simulation Results | 14 |
| S8.1 The Effects of the Genetic Architecture under Exponential Directional Selection . . | 14 |
| S8.2 Temporal Covariances and $G(t)$ under Gaussian Stabilizing Selection | 16 |
| S8.3 Convergence Correlations | 18 |
| S8.4 Sampling in Temporal Blocks | 21 |
| S8.5 Background Selection | 23 |
| S8.6 Truncation Selection | 24 |
| S8.7 The Effect of Fixations in the Empirical Datasets | 25 |
| S9 Additional Figures | 29 |
| S9.1 PCA of Barghi et al. (2019) replicates | 29 |
| S9.2 Bias Correction for Barghi et al. (2019) | 30 |
| S9.3 Barghi et al. (2019) Temporal Covariances Per Replicate | 31 |
| S9.4 Barghi et al. (2019) Trimmed Window Covariances | 32 |
| S9.5 Barghi et al. (2019) Empirical Null and Windowed Covariance Distributions | 33 |
| S9.6 Barghi et al. (2019) Tail Probabilities for Windowed Covariances Distributions . . . | 36 |

S1 Estimator Bias Correction

S1.1 Correcting variance bias with a single depth sampling process

Following Waples (1989), we have that the variance in allele frequency change at a locus in the initial generation, which is entirely due to a binomial sampling process, is $\text{Var}(p_0) = p_0(1-p_0)/d_0$ where d_0 is the number of binomial draws (e.g. read depth). At a later timepoint, the variance in allele frequency is a result of both the binomial sampling process at time t and the evolutionary process. Using the law of total variation we can partition the variation from each process,

$$\text{Var}(\tilde{p}_t) = \mathbb{E}(\text{Var}(\tilde{p}_t|p_t)) + \text{Var}(\mathbb{E}(\tilde{p}_t|p_t)) \quad (\text{S1})$$

$$= \underbrace{\frac{p_t(1-p_t)}{d_t}}_{\text{generation } t \text{ sampling noise}} + \underbrace{\text{Var}(p_t)}_{\text{variance due to evolutionary process}}. \quad (\text{S2})$$

Under a drift-only process, $\text{Var}(p_t) = p_0(1-p_0) \left[1 - \left(1 - \frac{1}{2N}\right)^t\right]$. However, with heritable variation in fitness, we need to consider the covariance in allele frequency changes across generations (Buffalo and Coop 2019). We can write

$$\text{Var}(p_t) = \text{Var}(p_0 + (p_1 - p_0) + (p_2 - p_1) + \dots + (p_t - p_{t-1})) \quad (\text{S3})$$

$$= \text{Var}(p_0 + \Delta p_0 + \Delta p_1 + \dots + \Delta p_{t-1}) \quad (\text{S4})$$

$$= \text{Var}(p_0) + \sum_{i=0}^{t-1} \text{Cov}(p_0, \Delta p_i) + \sum_{i=0}^{t-1} \text{Var}(\Delta p_i) + \sum_{0 \leq i < j}^{t-1} \text{Cov}(\Delta p_i, \Delta p_j). \quad (\text{S5})$$

Each allele frequency change is equally like to be positive as it is to be negative; thus by symmetry this second term is zero. Additionally $\text{Var}(p_0) = 0$, as we treat p_0 as a fixed initial frequency. We can write,

$$\text{Var}(p_t) = \sum_{i=0}^{t-1} \text{Var}(\Delta p_i) + \sum_{0 \leq i < j}^{t-1} \text{Cov}(\Delta p_i, \Delta p_j). \quad (\text{S6})$$

The second term, the cumulative impact of variance in allele frequency change can be partitioned into heritable fitness and drift components (Buffalo and Coop 2019; Santiago and Caballero 1995)

$$\text{Var}(p_t) = \sum_{i=0}^{t-1} \text{Var}(\Delta_D p_i) + \sum_{i=0}^{t-1} \text{Var}(\Delta_H p_i) + \sum_{0 \leq i < j}^{t-1} \text{Cov}(\Delta p_i, \Delta p_j). \quad (\text{S7})$$

where $\Delta_H p_t$ and $\Delta_D p_t$ indicate the allele frequency change due to heritable fitness variation and drift respectively. Then, sum of drift variances in allele frequency change is

$$\sum_{i=0}^{t-1} \text{Var}(\Delta_D p_i) = \sum_{i=0}^{t-1} \frac{p_i(1-p_i)}{2N} \quad (\text{S8})$$

replacing the heterozygosity in generation i with its expectation, we have

$$\sum_{i=0}^{t-1} \text{Var}(\Delta_D p_i) = p_0(1-p_0) \sum_{i=0}^{t-1} \frac{1}{2N} \left(1 - \frac{1}{2N}\right)^i \quad (\text{S9})$$

$$= p_0(1-p_0) \left[1 - \left(1 - \frac{1}{2N}\right)^t\right] \quad (\text{S10})$$

which is the usual variance in allele frequency change due to drift. Then, the total allele frequency change from generations 0 to t is $\text{Var}(\tilde{p}_t - \tilde{p}_0) = \text{Var}(\tilde{p}_t) + \text{Var}(\tilde{p}_0) - 2 \text{Cov}(\tilde{p}_t, \tilde{p}_0)$, where the covariance depends on the nature of the sampling plan (see Nei and Tajima 1981; Waples 1989). In the case where there is heritable variation for fitness, and using the fact that $\text{Cov}(\tilde{p}_t, \tilde{p}_0) = p_0(1-p_0)/2N$ for Plan I sampling procedures (Waples 1989), we write,

$$\text{Var}(\tilde{p}_t - \tilde{p}_0) = \text{Var}(\tilde{p}_t) + \text{Var}(\tilde{p}_0) - 2C \text{Cov}(\tilde{p}_t, \tilde{p}_0) \quad (\text{S11})$$

$$= \frac{p_t(1-p_t)}{d_t} + \frac{p_0(1-p_0)}{d_0} + p_0(1-p_0) \left[1 - \left(1 - \frac{1}{2N}\right)^t\right] + \quad (\text{S12})$$

$$\sum_{i=0}^{t-1} \text{Var}(\Delta_H p_i) + \sum_{0 \leq i < j}^{t-1} \text{Cov}(\Delta p_i, \Delta p_j) - \frac{C p_0(1-p_0)}{2N} \quad (\text{S13})$$

$$\frac{\text{Var}(\tilde{p}_t - \tilde{p}_0)}{p_0(1-p_0)} = 1 + \frac{p_t(1-p_t)}{p_0(1-p_0)d_t} + \frac{1}{d_0} - \left(1 - \frac{1}{2N}\right)^t + \quad (\text{S14})$$

$$\sum_{i=0}^{t-1} \frac{\text{Var}(\Delta_H p_i)}{p_0(1-p_0)} + \sum_{0 \leq i < j}^{t-1} \frac{\text{Cov}(\Delta p_i, \Delta p_j)}{p_0(1-p_0)} - \frac{C}{N} \quad (\text{S15})$$

where $C = 1$ if Plan I is used, and $C = 0$ if Plan II is used (see Waples 1989, p. 380 and Figure 1 for a description of these sampling procedures; throughout the paper we use sampling Plan II). Rearranging, we can create a bias-corrected estimator for the population variance in allele frequency change, and replace all population heterozygosity terms with the unbiased sample estimators, e.g. $\frac{d_t}{d_t-1} \tilde{p}_t(1-\tilde{p}_t)$,

$$\frac{d_0-1}{d_0} \frac{\text{Var}(\tilde{p}_1 - \tilde{p}_0)}{\tilde{p}_0(1-\tilde{p}_0)} - \frac{(d_0-1)}{d_0(d_1-1)} \frac{\tilde{p}_1(1-\tilde{p}_1)}{\tilde{p}_0(1-\tilde{p}_0)} - \frac{1}{d_0} + \frac{C}{N} = \frac{\text{Var}(\Delta_H p_0)}{p_0(1-p_0)} + \frac{1}{2N} \quad (\text{S16})$$

S1.2 Correcting variance bias with individual and depth sampling processes

Here, we extend the sampling bias correction described above to handle two binomial sampling processes: one as individuals are binomially sampled from the population, and another as reads are binomially sampled during sequencing. (see also Jónás et al. 2016). Let $X_t \sim \text{Binom}(n_t, p_t)$ where X_t is the count of alleles and n_t is the number of diploids sampled at time t . Then, these individuals are sequenced at a depth of d_t , and $Y_t \sim \text{Binom}(d_t, X_t/n_t)$ reads have the tracked allele. We let $\tilde{p}_t = Y_t/d_t$ be the observed sample allele frequency. Then, the sampling noise is

$$\text{Var}(\tilde{p}_t|p_t) = \mathbb{E}(\text{Var}(\tilde{p}_t|X_t)) + \text{Var}(\mathbb{E}(\tilde{p}_t|X_t)) \quad (\text{S17})$$

$$= p_t(1-p_t) \left(\frac{1}{n_t} + \frac{1}{d_t} - \frac{1}{n_t d_t} \right) \quad (\text{S18})$$

$$\text{Var}(\tilde{p}_t - \tilde{p}_0) = p_t(1-p_t) \left(\frac{1}{n_t} + \frac{1}{d_t} - \frac{1}{n_t d_t} \right) + p_0(1-p_0) \left(\frac{1}{n_0} + \frac{1}{d_0} - \frac{1}{n_0 d_0} \right) \quad (\text{S19})$$

$$- \frac{C p_0(1-p_0)}{N} + p_0(1-p_0) \left[1 - \left(1 - \frac{1}{2N} \right)^t \right] + \sum_{i=0}^{t-1} \text{Var}(\Delta_H p_i) \quad (\text{S20})$$

$$+ \sum_{0 \leq i < j}^{t-1} \text{Cov}(\Delta p_i, \Delta p_j) \quad (\text{S21})$$

Through the law of total expectation (see Kolaczowski et al. 2011 Supplementary File 1 for a sample proof), one can find that an unbiased estimator of the half the heterozygosity is

$$\frac{n_t d_t}{(n_t - 1)(d_t - 1)} \tilde{p}_t(1 - \tilde{p}_t). \quad (\text{S22})$$

Replacing this unbiased estimator for half of the heterozygosity into our expression above, the total sample variance is

$$\text{Var}(\tilde{p}_t - \tilde{p}_0) = \frac{n_t d_t \tilde{p}_t(1 - \tilde{p}_t)}{(n_t - 1)(d_t - 1)} \left(\frac{1}{n_t} + \frac{1}{d_t} - \frac{1}{n_t d_t} \right) + \frac{n_0 d_0 \tilde{p}_0(1 - \tilde{p}_0)}{(n_0 - 1)(d_0 - 1)} \left(\frac{1}{n_0} + \frac{1}{d_0} - \frac{1}{n_0 d_0} \right) + \quad (\text{S23})$$

$$\begin{aligned} & \frac{n_0 d_0 \tilde{p}_0(1 - \tilde{p}_0)}{(n_0 - 1)(d_0 - 1)} \left[1 - \left(1 - \frac{1}{2N} \right)^t \right] - \frac{C}{N} \frac{n_0 d_0 \tilde{p}_0(1 - \tilde{p}_0)}{(n_0 - 1)(d_0 - 1)} + \\ & \sum_{i=0}^{t-1} \text{Var}(\Delta_H p_i) + \sum_{0 \leq i < j}^{t-1} \text{Cov}(\Delta p_i, \Delta p_j). \end{aligned} \quad (\text{S24})$$

As with equation (S16), we can rearrange this to get a biased-corrected estimate of the variance in allele frequency change between adjacent generations, $\text{Var}(\Delta p_t)$.

S1.3 Covariance Correction

We also need to apply a bias correction to the temporal covariances (and possibly the replicate covariances if the initial sample frequencies are all shared). The basic issue is that $\text{Cov}(\Delta \tilde{p}_t, \Delta \tilde{p}_{t+1}) = \text{Cov}(\tilde{p}_{t+1} - \tilde{p}_t, \tilde{p}_{t+2} - \tilde{p}_{t+1})$, and thus shares the sampling noise of timepoint $t+1$. Thus acts to bias the covariance by subtracting off the noise variance term of $\text{Var}(\tilde{p}_{t+1})$, so we add the expectation of this bias, derived above, back in. We discuss this in more detail below in deriving the bias correction for the temporal-replicate variance covariance matrix.

S1.4 Temporal-Replicate Covariance Matrix Correction

In practice, we simultaneously estimate the temporal and replicate covariance matrices for each replicate, which we call the temporal-replicate covariance matrix. This needs a bias correction; we extend the bias corrections for single locus variance and covariance described in Supplementary Material Sections S1.1, S1.2, and S1.3 to multiple sampled loci and the temporal-replicate covariance matrix here. With frequency data collected at $T + 1$ timepoints across R replicate populations at L loci, we have multidimensional arrays \mathbf{F} of allele frequencies, \mathbf{D} of sequencing depths, and \mathbf{N} of the number of individuals sequenced, each of dimension $R \times (T + 1) \times L$. We calculate the array $\Delta\mathbf{F}$ which contains the allele frequency changes between adjacent generations, and has dimension $R \times T \times L$. The operation $\text{flat}(\Delta\mathbf{F})$ flattens this array to a $(R \cdot T) \times L$ matrix, such that rows are grouped by replicate, e.g. for timepoint t , replicate r , and locus l such that for allele frequencies $p_{t,r,l}$, the frequency change entries are

$$\text{flat}(\Delta\mathbf{F}) = \begin{bmatrix} \Delta p_{1,0,0} & \Delta p_{2,0,0} & \cdots & \Delta p_{1,1,0} & \Delta p_{2,1,0} & \cdots & \Delta p_{T,R,0} \\ \Delta p_{1,0,1} & \Delta p_{2,0,1} & \cdots & \Delta p_{1,1,1} & \Delta p_{2,1,1} & \cdots & \Delta p_{T,R,1} \\ \vdots & \vdots & \ddots & \vdots & \vdots & \ddots & \vdots \\ \Delta p_{1,0,L} & \Delta p_{2,0,L} & \cdots & \Delta p_{1,1,L} & \Delta p_{2,1,L} & \cdots & \Delta p_{T,R,L} \end{bmatrix} \quad (\text{S25})$$

where each $\Delta p_{t,r,l} = p_{t+1,r,l} - p_{t,r,l}$. Then, the sample temporal-replicate covariance matrix \mathbf{Q}' calculated on $\text{flat}(\Delta\mathbf{F})$ is a $(R \cdot T) \times (R \cdot T)$ matrix, with the R temporal-covariance block submatrices along the diagonal, and the $R(R - 1)$ replicate-covariance submatrices matrices in the upper and lower triangles of the matrix,

$$\mathbf{Q}' = \begin{bmatrix} \mathbf{Q}'_{1,1} & \mathbf{Q}'_{1,2} & \cdots & \mathbf{Q}'_{1,R} \\ \mathbf{Q}'_{2,1} & \mathbf{Q}'_{2,2} & \cdots & \mathbf{Q}'_{2,R} \\ \vdots & \vdots & \ddots & \vdots \\ \mathbf{Q}'_{R,1} & \mathbf{Q}'_{R,2} & \cdots & \mathbf{Q}'_{R,R} \end{bmatrix} \quad (\text{S26})$$

where each submatrix $\mathbf{Q}'_{i,j}$ ($i \neq j$) is the $T \times T$ sample replicate covariance matrix for replicates i and j , and the submatrices along the diagonal $\mathbf{Q}'_{r,r}$ are the temporal covariance matrices for replicate r .

Given the bias of the sample covariance of allele frequency changes, we calculated an expected bias matrix \mathbf{B} , averaging over loci,

$$\mathbf{B} = \frac{1}{L} \sum_{l=1}^L \frac{\mathbf{h}_l}{2} \circ \left(\frac{1}{\mathbf{d}_l} + \frac{1}{2\mathbf{n}_l} + \frac{1}{2\mathbf{d}_l \circ \mathbf{n}_l} \right) \quad (\text{S27})$$

where \circ denotes elementwise product, and \mathbf{h}_l , \mathbf{d}_l , and \mathbf{n}_l , are rows corresponding to locus l of the unbiased heterozygosity arrays \mathbf{H} , depth matrix \mathbf{D} , and number of diploids matrix \mathbf{N} . The unbiased $R \times (T + 1) \times L$ heterozygosity array can be calculated as

$$\mathbf{H} = \frac{2\mathbf{D} \circ \mathbf{N}}{(\mathbf{D} - 1) \circ (\mathbf{N} - 1)} \circ \mathbf{F} \circ (1 - \mathbf{F}) \quad (\text{S28})$$

where division here is elementwise. Thus, \mathbf{B} is a $R \times (T+1)$ matrix. As explained in Supplementary Material Section S1.2 and S1.3, the temporal variances and covariances require bias corrections, meaning each temporal covariance submatrix $\mathbf{Q}_{r,t}$ requires two corrections. For an element $Q_{r,t,s} = \text{Cov}(\Delta p_t, \Delta p_s)$ of the temporal covariance submatrix for replicate r , $\mathbf{Q}_{r,t}$, we apply the following correction

$$Q_{r,t,s} = \begin{cases} Q'_{r,t,s} - b_{r,t} - b_{r,t+1}, & \text{if } t = s \\ Q'_{r,t,s} + b_{r,\max(t,s)}, & \text{if } |t - s| = 1 \end{cases} \quad (\text{S29})$$

where $b_{r,t}$ is element in row r and column t of \mathbf{B} .

S2 Barghi et al. (2019) Temporal Covariances

Since each replicate population was sequenced every ten generations, the timepoints $t_0 = 0$ generations, $t_1 = 10$ generations, $t_2 = 20$ generations, etc., lead to observed allele frequency changes across ten generation blocks, $\Delta p_{t_0}, \Delta p_{t_1}, \dots, \Delta p_{t_6}$. Consequently, the ten temporal covariance matrices for each of the ten replicate populations have off-diagonal elements of the form $\text{Cov}(\Delta p_{t_0}, \Delta p_{t_1}) = \text{Cov}(p_{t_1} - p_{t_0}, p_{t_2} - p_{t_1}) = \sum_{i=0}^{10} \sum_{j=10}^{20} \text{Cov}(\Delta p_i, \Delta p_j)$. Each diagonal element has the form $\text{Var}(\Delta p_{t_0}) = \sum_{i=0}^{t_0-1} \text{Var}(\Delta p_i) + \sum_{i=0}^{t_0-1} \sum_{j \neq i}^{t_0-1} \text{Cov}(\Delta p_i, \Delta p_j)$, and is thus a combination of the effects of drift and selection, as both the variance in allele frequency changes and cumulative temporal autocovariances terms increase the variance in allele frequency. With sampling each generation, one could more accurately partition the total variance in allele frequency change (Buffalo and Coop 2019); while we cannot directly estimate the contribution of linked selection to the variance in allele frequency change here, the presence of a positive observed covariance between allele frequency change can only be caused linked selection.

S3 Block Bootstrap Procedure

The estimators used in this paper are predominantly ratios, e.g. temporal-replicate covariance standardized by half the heterozygosity, $G(t)$ which is the ratio of cumulative covariance to total variance, and the convergence correlation (equation (2)). In these cases, we can exploit the linearity of the expectation to make the bootstrap procedure more computationally efficient, by pre-calculating the statistics of the ratio's numerator and denominator, $N(\mathbf{x}_i)$ and $D(\mathbf{x}_i)$, on the data \mathbf{x}_i for all blocks $i \in \{1, 2, \dots, W\}$ in the genome. Then we draw W bootstrap samples with replacement, and compute the estimate for bootstrap sample b with an average weighted by the fraction w_i of total loci contained in each block,

$$\tilde{\theta}_b = \frac{\sum_{i=1}^W w_i N(\mathbf{x}_i)}{\sum_{i=1}^W w_i D(\mathbf{x}_i)} \quad (\text{S30})$$

Note that computing the ratio of averages rather than the average of a ratio is a practice common for population genetic statistics like F_{ST} (Bhatia et al. 2013). With these B bootstrap estimates, we calculate the $\alpha/2$ and $1 - \alpha/2$ quantiles, which we use to estimate the $1 - \alpha = 95\%$ pivot confidence intervals (p. 33 Wasserman 2006, p. 194 Davison and Hinkley 2013) throughout the paper,

$$C_\alpha = \left(2\hat{\theta} - q_{1-\alpha/2}, 2\hat{\theta} - q_{\alpha/2} \right). \quad (\text{S31})$$

where $\hat{\theta}$ is the estimate, and q_x is bootstrap quantile for probability x .

S4 Replicate $G(t)$ and Partitioning the Variance in Allele Frequency

We define a statistic similar to $G(t)$ for estimating the proportion of allele frequency change common between two replicate populations due to linked selection. Covariance in allele frequency change between two replicate populations is due to convergent selection pressure selecting haplotypes shared between the two replicate populations, which acts to perturb linked neutral variation in parallel way.

$$G_R(t) = \frac{\mathbb{E}_{A \neq B}(\sum_{i \neq j}^t \text{Cov}(\Delta p_{i,A}, \Delta p_{j,B}))}{\mathbb{E}_R(\text{Var}(p_{t,R} - p_{0,R}))} \quad (\text{S32})$$

where $\mathbb{E}_{A \neq B}$ indicates that the expectation is taken over all ordered pairs of replicates (e.g. summing all off-diagonal elements replicate covariances), and \mathbb{E}_R indicates taking expectation over all replicates. This measures the fraction of variance in allele frequency change (averaged across replicates) due to shared selection pressure.

Extending our theoretic work in Buffalo and Coop (2019), we can partition the allele frequency change in two replicates into drift, and shared selection and replicate-specific selection components of allele frequency change. For two replicates, A and B ,

$$\Delta p_{t,A} = \Delta_D p_{t,A} + \Delta_U p_{t,A} + \Delta_S p_t \quad (\text{S33})$$

$$\Delta p_{t,B} = \Delta_D p_{t,B} + \Delta_U p_{t,B} + \Delta_S p_t \quad (\text{S34})$$

where $\Delta_D p_{t,A}$ is allele frequency change due to drift (this is specific to a replicate, and equal to $\Delta_N p_{t,A} + \Delta_M p_{t,A}$ in the notation of Buffalo and Coop 2019), $\Delta_U p_{t,A}$ is the allele frequency change from indirect selection specific to replicate A (and likewise with $\Delta_U p_{t,A}$ for replicate B), and $\Delta_S p_t$ is the allele frequency change from indirect selection shared across the replicates A and B (this term lacks a replicate subscript since by construction it is identical between replicates). By construction, each of these terms is uncorrelated, so the variance can be written as:

$$\text{Var}(\Delta p_{t,A}) = \text{Var}(\Delta_D p_{t,A}) + \text{Var}(\Delta_U p_{t,A}) + \text{Var}(\Delta_S p_t) \quad (\text{S35})$$

$$(\text{S36})$$

The shared effects of indirect selection can be quantified from the observed allele frequency changes, since the covariance in allele frequency change across replicates is the covariance of the shared term by construction,

$$\text{Cov}(\Delta p_{t,A}, \Delta p_{t,B}) = \text{Cov}(\Delta_S p_t, \Delta_S p_t) = \text{Var}(\Delta_S p_t) \quad (\text{S37})$$

In artificial selection studies with a control (non-selected) line, such as the Castro et al. (2019) study, this allows us to estimate the contribution of the effects of shared and unique indirect selection. In the case of this study, we can estimate the drift, unique selection effect, and shared selection effect terms using the fact that,

$$\Delta p_{t,LS1} = \Delta_D p_{t,LS1} + \Delta_U p_{t,LS1} + \Delta_{LS} p_t \quad (\text{S38})$$

$$\Delta p_{t,LS2} = \Delta_D p_{t,LS2} + \Delta_U p_{t,LS2} + \Delta_{LS} p_t \quad (\text{S39})$$

$$\Delta p_{t,Ctrl} = \Delta_D p_{t,Ctrl}. \quad (\text{S40})$$

Note that since the control replicate does not undergo artificial selection, we assume that its allele frequency changes are determined entirely by genetic drift. With free mating individuals (such as in a cage population), this may not be the case, and sequencing adjacent generations would allow one to differentiate the effects of selection and drift.

We assume that we can approximate the contribution of genetic drift in the Longshanks selection lines with the observed variance in the control line, or $\text{Var}(\Delta p_{t,Ctrl}) = \text{Var}(\Delta_{Dp_{t,LS1}}) = \text{Var}(\Delta_{Dp_{t,LS2}})$. Then, the combined effects of selection can be estimated by averaging the variances of the two Longshanks selection lines, and subtracting the variance in allele frequency change in the control line, which we treat as driven by drift alone (since matings are random). Note that each variance is bias-corrected according to the methods described in Supplementary Materials S1.4, and the average sequencing depths between lines are nearly identical. Thus, we have

$$(\text{Var}(\Delta p_{t,LS1}) + \text{Var}(\Delta p_{t,LS2}))/2 - \text{Var}(\Delta p_{t,Ctrl}) = \overline{\text{Var}(\Delta_U p_{t,LS})} + \text{Var}(\Delta_{LS} p_t) \quad (\text{S41})$$

where the bar indicates values averaged both Longshanks selection lines. Additionally, use the fact that

$$\text{Cov}(\Delta p_{t,LS1}, \Delta p_{t,LS2}) = \text{Var}(\Delta_{LS} p_t) \quad (\text{S42})$$

we can also separate out the unique and shared components by subtracting off this covariance,

$$\overline{\text{Var}(\Delta_U p_{t,LS})} = (\text{Var}(\Delta p_{t,LS1}) + \text{Var}(\Delta p_{t,LS2}))/2 - \text{Var}(\Delta p_{t,Ctrl}) - \text{Cov}(\Delta p_{t,LS1}, \Delta p_{t,LS2}). \quad (\text{S43})$$

Finally, we can divide each of these values by the total variance to get the proportion of total variance drift, and unique and shared effects of selection contribute towards the total. To derive confidence intervals for the estimates of unique and shared effects of selection, we use a block bootstrap procedure as described in Supplementary Materials Section S3.

S5 The Empirical Neutral Null Windowed Covariance Distribution

To detect an excess of genomic regions with unusually high or low covariances, we need to compare the distribution of observed windowed covariances to a null distribution of windowed covariances that we would expect under no selection. While we could construct a theoretic sampling distribution of the spurious covariances created by neutral genetic drift at particular site, the unknown linkage disequilibrium between sites would mean that this is not an adequate null model for the distribution of windowed covariances in our data.

To address this limitation, we construct a neutral null model by sign-permuting the observed allele frequency changes. This destroys the covariances built up by selection, mimicking a neutral allele's frequency trajectory. This approach is conservative, since selection also acts to increase the magnitude of allele frequency changes (see equation 1 of Buffalo and Coop 2019), but this magnitude is not affected by the sign-permutation procedure. Consequently, the resulting empirical null distribution has higher variance than would be expected under neutrality alone.

Still, we wanted to ensure that LD between sign-permuted blocks, which will affect the variance of the empirical null distribution, does not impact our primary finding that the distribution of temporal covariances becomes increasingly negative in the Barghi et al. (2019) dataset through time. To address this, we also sign-permuted at the whole chromosome level finding we recapitulate the same pattern (Supplementary Figure S29).

S6 Bergland et al. (2014) Re-Analysis

We also applied our temporal covariance approach to Bergland et al. (2014), which found evidence of genome-wide fluctuating selection between Spring and Fall seasons across three years *Drosophila melanogaster*. As described in Buffalo and Coop (2019), if fluctuating selection pressure among time-periods are the dominant genome-wide pattern, we might expect positive covariances between like seasons changes (e.g. Spring 2010 to Fall 2010 and Spring 2011 to Fall 2011), and negative covariances between dislike seasonal changes (e.g. Fall 2009 to Spring 2010 and Fall 2010 to Spring 2011). However, while we find temporal covariances that are non-zero, we find only weak support for a seasonal fluctuating model driving these covariances. In Supplementary Figure S1, we show the temporal covariances from varying reference generations, across seasonal transitions that are alike (e.g. the covariance between the allele frequency changes between Fall 2009 and Spring 2009, and frequency changes between Fall 2010 and Spring 2010), and dislike (e.g. the covariance between the allele frequency change between Fall 2009 and Spring 2009, and the frequency changes between Spring 2010 and Fall 2009). The first row of temporal covariance matrix is consistent with fluctuating selection operating for two timepoints, as the first covariance is negative, and the second is positive, and later covariances are not statistically differentiable from zero (which could occur if LD and additive genetic variance decay). However, all other temporal covariances do not fit the pattern we would expect under genome-wide fluctuating selection.

We wanted to establish that our temporal-covariance matrix bias correction was working correctly. We find that it corrects the relationship between depth and both variance and covariance (Supplementary Figure S4) as expected.

It is unclear how strong the fluctuations would have to be to generate a genome-wide average signal of fluctuating selection from temporal covariances. For example, many loci could still show

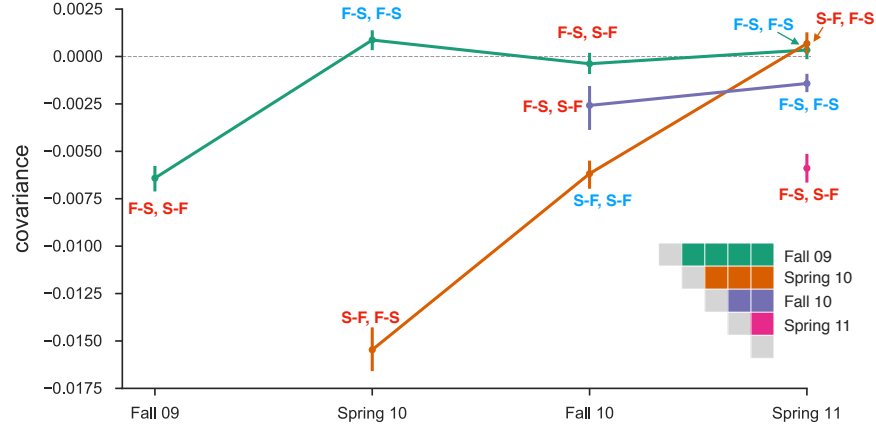


Figure S1: Temporal covariances from the Bergland et al. (2014) study, from varying reference generations (e.g. rows along the temporal covariance matrix). Each covariance is labeled indicating whether the covariance is between two like seasonal transitions (e.g. the covariance between allele frequency changes from fall to spring in one year, and fall to spring in another) or two dislike seasons (e.g. the covariance between fall to spring in one year, and spring to fall in another year). Covariances between like transitions are expected to be positive when there is a genome-wide effect of fluctuating selection (and these labels are colored blue), while covariances between dislike transitions are expected to be negative (and these labels are colored red). 95% confidence intervals were constructed by a block-bootstrapping procedure where the blocks are megabase tiles.

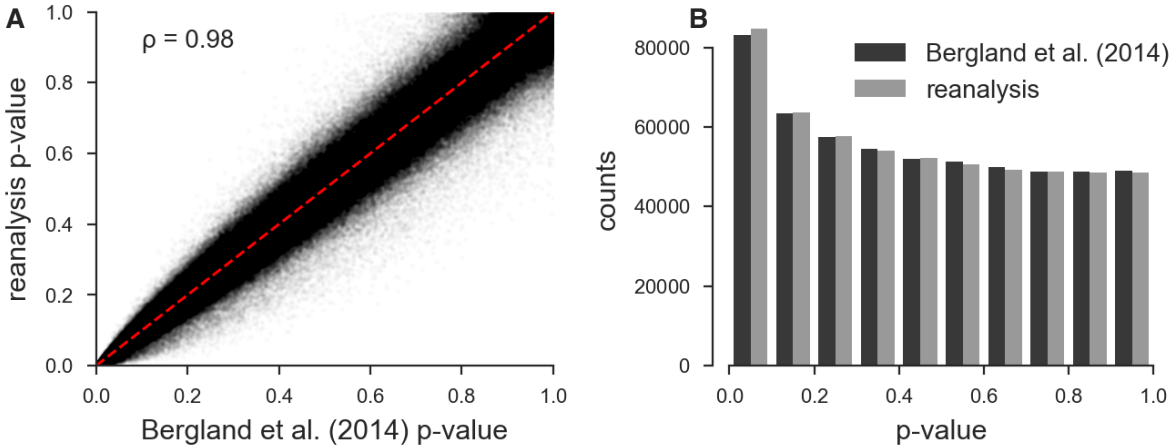


Figure S2: **A:** Scatterplot of the original unadjusted p-values from Bergland et al. (2014) and the p-values from our reanalysis of the same data using the same statistical methods; the minor discrepancy is likely due to software version differences. **B:** The histograms of the p-values of our reanalysis and the original Bergland et al. (2014) data; again the minor discrepancy is likely due to software differences. Overall, our implementation of Bergland et al.'s statistical methods produces results very close to the original analysis.

a signal of fluctuating selection, but the average signal could be overwhelmed by other signals of other selection. To investigate whether there was a genome-wide excess of loci showing evidence of fluctuating selection we reanalyzed the data of (Bergland et al. 2014) using the same seasonal fluctuating model as the original paper. This model is a Binomial logit-linked GLM fit per-locus, where the frequencies are regressed on the Spring/Fall seasons are encoded as a dummy variable. We use the same binomial weighting procedure as Bergland et al. (2014), where the weights are determined by the effective number of chromosomes, $N_{eff} = (2n_t d_t - 1)/(2n_t + d_t)$ (n_t and d_t are the number of diploid individuals and the read depth at timepoint t , respectively). We fit this model on all loci marked as used in the VCF provided with the Bergland et al. (2014) study (doi:10.5061/dryad.v883p). Overall, our p-values for the Wald test for each locus closely match those of the original paper (Pearson correlation coefficient 0.98, p-value $< 2.2 \times 10^{-16}$; see Supplementary Figure S2 A), and the histograms of the p-values are nearly identical (Supplementary Figure S2 B). Bergland et al. (2014) find loci with a significant association with season after a Benjamini and Hochberg FDR p-value adjustment (Benjamini and Hochberg 1995), however, the null hypothesis of the Wald test does not give us an idea of the expected number of variants that may spuriously fit the pattern of seasonal fluctuating selection as it does not account for genetic drift or other forms of hitchhiking.

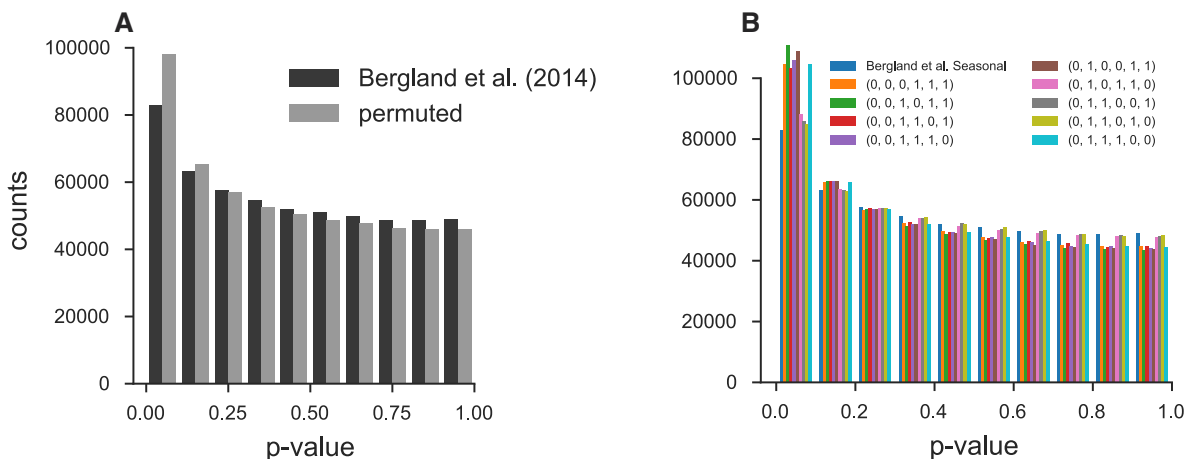


Figure S3: **A:** Histogram of original Bergland et al. (2014) seasonal p-values and p-values creating by randomly permuting the seasons at each locus. **B:** Histogram of original Bergland et al. (2014) p-values alongside all unique permutations (ignoring symmetries that lead to identical p-values).

To investigate whether there is a genome-wide evidence of an enrichment of fluctuating selection we created an empirical null distribution by randomly permuting the season labels and re-running the per-locus seasonal GLM model, as proposed by Machado et al. (2018). We find, regardless of whether we permute at the locus-level or the permutation replicate-level, that the observed seasonal p-value distribution Bergland et al. (2014) is not enriched for significant p-values beyond what we would expect from the permutation null. In fact, there appears there is more enrichment for low p-values when seasonal labels are randomly permuted (Supplementary Figure S3, suggesting by random chance we might expect more variants with a seasonal fluctuating pattern than found in the original Bergland et al. (2014) study. While surprising, this could be explained by the presence of temporal structure across the samples not consistent with seasonal fluctuating selection. Some

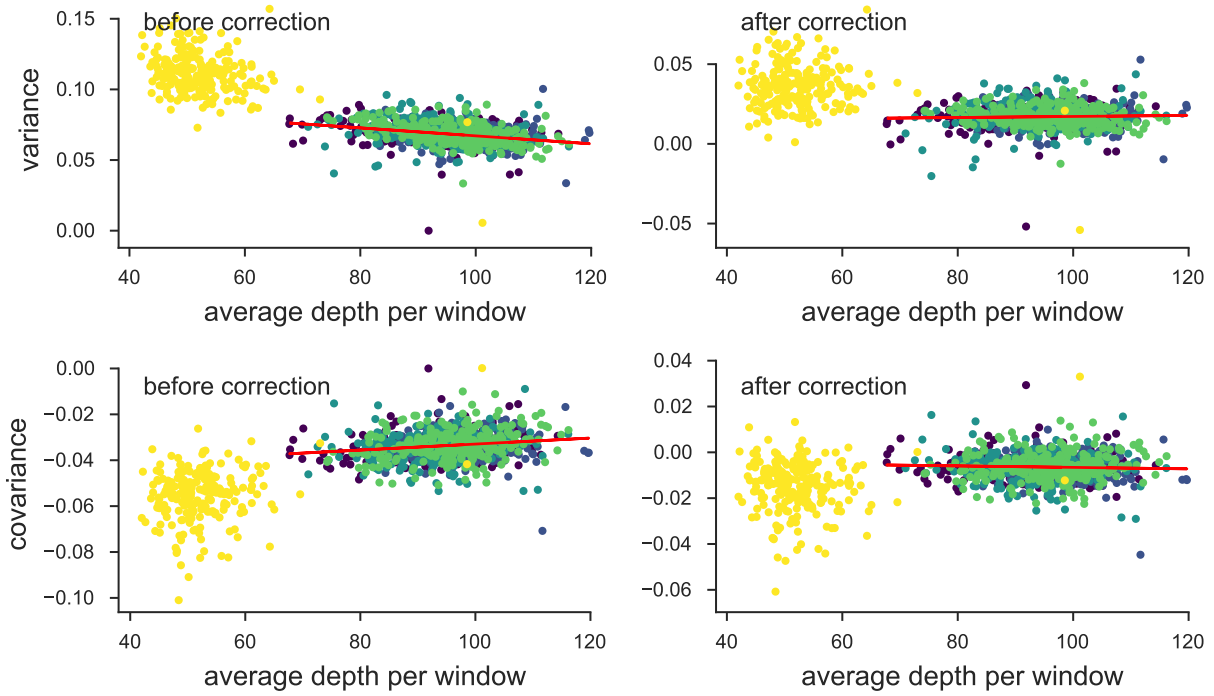


Figure S4: The variance and covariances from the Bergland et al. (2014) study, calculated in 100kb genomic windows plotted against average depth in a window before and after bias correction. Each panel has a least-squares estimate between the variance and covariance, and the average depth. The bias correction procedure is correcting sampling bias in both the variance and covariance such that the relationship with depth is constant. Colors indicate the different chromosomes of *D. melanogaster*; we have excluded the X chromosome (yellow points; chromosome 4 was not in the original study) from the regression due to large differences in average coverage.

fraction of the permutations happen to fit non-seasonal structure well, leading to an enrichment of small p-values. We note that genetic drift is not accounted for in the model used to estimate the significance of seasonally fluctuations and so some of these issues from non-seasonal structure may be due to a poorly calibrated null model. Furthermore, non-seasonal temporal structure is also evident in our temporal covariances (Supplementary Figure S1), where we see strong evidence of selection (non-zero temporal covariances), yet the pattern does not follow that of seasonal fluctuating selection.

S7 Approximating the Reduction in Diversity from $G(t)$

To help reconcile our measure of linked selection, $G(t)$, with familiar expressions as a reduction in neutral diversity, as parameterized by N_e , we develop some rough approximations here. Note, however, that since linked selection generates temporal covariance, the overall effect is qualitatively different than just a simple reduction in N_e , as drift alone cannot generate temporal covariances. First, we introduce some convenient notation. Let $V_T = \text{Var}(p_t - p_0)$ be the total observed *variance* in allele frequency, $C_{LS} = \sum_{i=0}^{t-1} \sum_{j \neq i}^{t-1} \text{Cov}(\Delta p_i, \Delta p_j)$ be the contribution of all pairwise temporal

covariances (observable), V_D be the unobservable drift-only variance in allele frequency, and $V_{LS} = \sum_{i=0}^{t-1} \text{Var}(\Delta_{LS} p_i)$ which is the (unobservable) effect linked selection has on the variances in allele frequency change. Then,

$$V_T = V_{LS} + C_{LS} + V_D. \quad (\text{S44})$$

Our measure $G(t)$ is then,

$$G(t) = \frac{C_{LS}}{V_T}, \quad (\text{S45})$$

meaning we can express the fraction of total variance due to drift alone as

$$\frac{V_D}{V_T} = 1 - G(t) - \frac{V_{LS}}{V_T} \quad (\text{S46})$$

$$= 1 - G(t) - \varepsilon \quad (\text{S47})$$

$$\leq 1 - G(t), \quad (\text{S48})$$

where $\varepsilon \geq 0$ since these variances are positive. Throughout this section, for convenience, we assume that the covariances contributing to C_{LS} , and thus $G(t)$, are all positive.

Rather than expressing this relationship in terms of variances in allele frequencies, we can express the same relationship in terms of N_e . In a neutral Wright–Fisher population, the total variation in allele frequency change over t generations is

$$V_T = \text{Var}(p_t - p_0) = p_0(1 - p_0) [1 - (1 - 1/2N_e)^t]. \quad (\text{S49})$$

For small t , a common temporal estimator for the variance effective population size N_e is,

$$N_e \approx \frac{tp_0(1 - p_0)}{2V_T}. \quad (\text{S50})$$

Then, the drift-only N_e estimate (that is, removing the effects of linked selection) replaces the observable V_T with unobservable V_D , and uses the $G(t)$ estimate to bound this:

$$N_{e,D} \approx \frac{tp_0(1 - p_0)}{2V_T(1 - G(t) - \varepsilon)} \quad (\text{S51})$$

$$\geq \frac{tp_0(1 - p_0)}{2V_T(1 - G(t))} \quad (\text{S52})$$

$$\geq \frac{N_e}{1 - G(t)} \quad (\text{S53})$$

$$\frac{N_e}{N_{e,D}} \lesssim 1 - G(t) \quad (\text{S54})$$

In the linked selection literature, it is common to translate the impact of linked selection as a reduction in the level of neutral pairwise diversity in the absence of linked selection, π_0 . Under the coalescent, $\pi_0 = 2\mu\mathbb{E}(T_2)$ where $\mathbb{E}(T_2)$ is the pairwise time to coalescence, which under drift alone in a constant population of size N_e , is $\mathbb{E}(T_2) = 2N$. The fraction of neutral diversity (in the absence of linked selection) reduced by selection is then, $1 - \bar{\pi}/\pi_0$, or equivalently, $1 - N_e/N_{e,D}$. Then,

$$G(t) \lesssim 1 - \frac{N_e}{N_{e,D}}, \quad (\text{S55})$$

which shows that our measure $G(t)$ is a lower bound, over much shorter timescales, to the familiar measure $1 - \bar{\pi}/\pi_0$.

Elyashiv et al. (2016) estimated that linked selection in *Drosophila melanogaster* had resulted in a $1 - \bar{\pi}/\pi_0 = 77\%$ reduction in the level of neutral diversity. Thus our estimate of $G(t) \approx 20\%$ in *Drosophila simulans* is smaller than that seen over long timespans in a closely related species.

S8 Simulation Results

We conducted extensive simulations to understand how temporal covariance, $G(t)$, and convergence correlations behave under (1) different quantitative genetic fitness models, (2) different trait architectures (e.g. varying levels of V_A for fitness and the number of sites affecting fitness), (3) background selection, and (4) different sampling periods. Furthermore, we use two replicate population simulations to investigate how convergence correlations depend on (1) the population sizes of each selection line sampled from the main population, and (2) the direction the trait is selected on in each line (i.e. in the same direction, differing directions, or only one line selected).

Due to the high computational burden of forward simulations over this wide breadth of parameters, we modeled a single 50 megabase region in a population of $N = 1000$ diploid individuals with a neutral variant mutation rate of 10^{-8} and a recombination rate of 10^{-8} per basepair. This is roughly analogous to a quarter of an autosome of *Drosophila melanogaster*; however with this small population size and mutation rate, the population mutation rate θ for the entire region leads to far fewer neutral sites to calculate covariances and other statistics on than expected for a region this length in *D. melanogaster*. Since our main goal is to understand the dynamics of statistics used in the paper and how they are affected by different quantitative genetic fitness models, background selection, and trait architecture, we use population frequencies rather than sampling frequencies.

All forward simulations were conducted using SLiM (Haller and Messer 2019) and run and processed using Snakemake (Köster and Rahmann 2012); all simulation routines are available in the Github repository <https://github.com/vsbuffalo/cvtk/>.

S8.1 The Effects of the Genetic Architecture under Exponential Directional Selection

We first investigated the effects of the selected trait’s genetic architecture on temporal covariances and $G(t)$ by neutrally burning in a population for $10N$ generations, and selecting on the trait with an exponential fitness function (*where fitness of a trait value z is $w(z) \propto \exp(z)$*). The exponential fitness function corresponds to multiplicative selection across sites and so serves as the simplest directional selection model of a trait to understand the effects of genetic architecture on the statistics we have used in the paper.

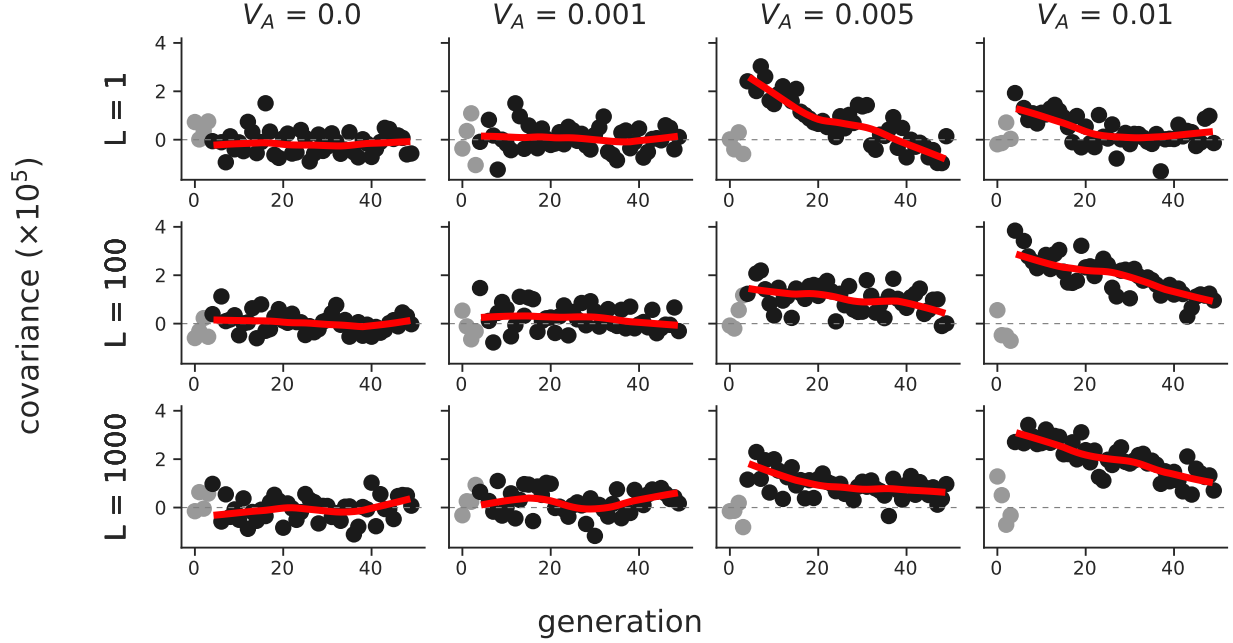


Figure S5: The temporal covariances $\text{Cov}(\Delta p_5, \Delta p_t)$ from the onset of selection (generation 5) to a later time point t , which varies along the x-axis, across a variety of different *initial* trait additive genetic variances (V_A , columns) and number of sites contributing to the trait (L , rows). Each point is the temporal covariance averaged over 50 replicate simulations; dark gray points are temporal covariances after the onset of selection, and light gray points are before. The red line is a loess-smoothed curve through the covariances after the onset of selection. Selection on the trait was imposed through an exponential fitness function.

During this burnin, sites were either marked as neutral (with mutation rate $\mu_{\text{neutral}} = 10^{-8}$ per gamete per generation) or contributed to the trait's value (with mutation rate μ_{trait}), but were not selected until generation $10N + 5$ (the five generations after burnin serve as a neutral control). The trait mutation rate, μ_{trait} was set by targeting a particular architecture, the number of selected sites, L . Each site contributing to the trait's value was randomly chosen to have effect size $\pm\alpha$ with equal probability, where α was set to target a particular additive genetic variance for the trait, V_A , for the target number of selected sites L .

Overall, we *again see a* finding of Buffalo and Coop (2019): that the initial expected temporal covariance conditioned on V_A , is invariant to the number of loci determining the trait's value, L (Supplementary Figure S5). We do find some evidence that the decay in temporal covariance is faster when the trait has a monogenic basis (see the third column of Supplementary Figure S5); this is expected *since* the selection coefficients are larger for these monogenic simulations, leading to faster allele frequency changes and a rapid change in additive genetic variance.

In our previous work, we did not investigate the affect of trait architecture on our measure $G(t)$. Using the exponential fitness function simulations, we also calculated $G(t)$ for each of the replicate simulations. We find that the $G(t)$ trajectories can vary considerably across replicates depending on the number of sites (L) determining the trait's value (Supplementary Figure S6). When a trait is reasonably monogenic ($L \approx 1$), $G(t)$ trajectories vary considerably across replicate lines, as certain lines may stochastically lose the few copies of the selected alleles (top row of Supplementary Figure

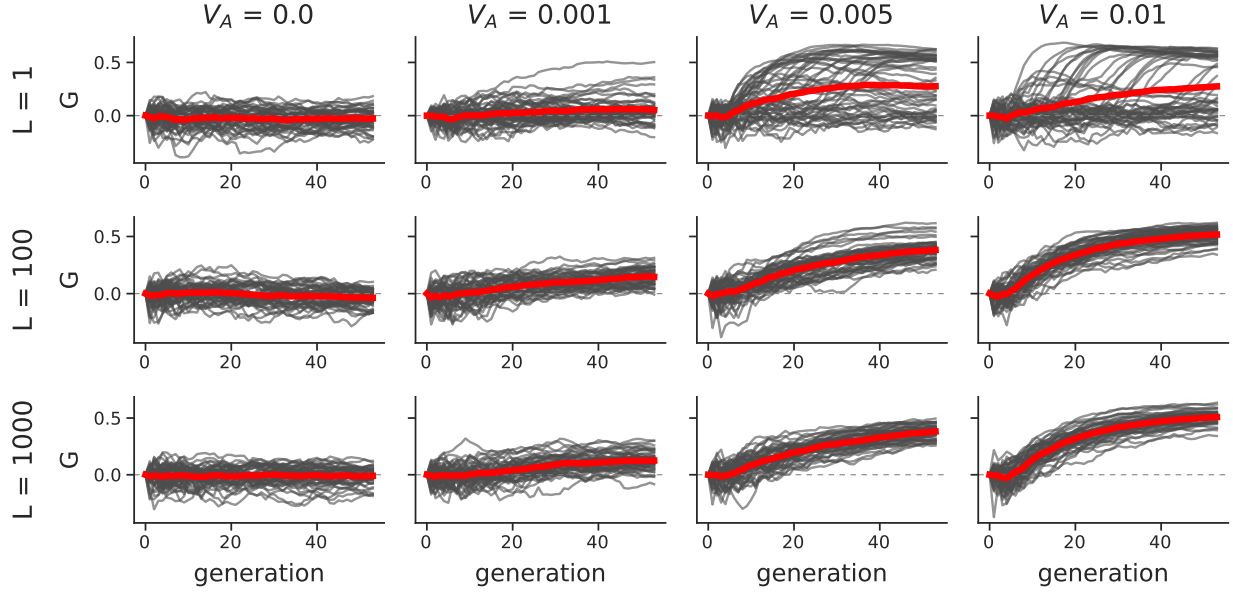


Figure S6: The $G(t)$ trajectories of 50 replicate simulations, across different trait architectures (L is the target number of sites affecting the trait’s value, and V_A is the target trait additive genetic variance). The red line is the mean trajectory across all replicate simulations. Like Supplementary Figure S5, the onset of selection is five generations after the $10N$ generation burnin; this is evident by the initial flat period of the $G(t)$ trajectory.

S6). However, with a polygenic trait, ($L \geq 100$), the $G(t)$ trajectories across replicates are similar as each replicate contains an abundance of trait alleles (bottom rows of Supplementary Figure S6). Comparing the simulated $G(t)$ replicate trajectories of Supplementary Figure S6 with the Barghi et al. (2019) $G(t)$ trajectories in Figure 1B, we again confirm a finding of Barghi et al. (2019): that there is considerable genetic redundancy among beneficial alleles, meaning because of the polygenic architecture, there are multiple routes to adaptation. We should note that our simplified simulation routines are slightly different from the Barghi et al. (2019) study in that the burnin populations are all independent; however we expect the same qualitative result.

S8.2 Temporal Covariances and $G(t)$ under Gaussian Stabilizing Selection

Additionally, we wanted to ensure that our temporal covariances and $G(t)$ trajectories were robust to more complicated, but realistic fitness models. To this end, we also simulated Gaussian stabilizing selection (GSS) on a trait during burnin, followed by one of two optimum shift routines: (1) sudden optima shifts of $\mu_{\text{sudden}} = \{0.1, 0.5, 1\}$, and (2) very graduate optima shifts of $\mu_{\text{gradual}} = \{0.001, 0.01\}$ per generation using the same two population simulation scheme described above (these shifts are in standard deviations, since $V_S = 1$). We used a polygenic architecture for these simulations, with trait alleles assigned a ± 0.01 effect size with equal probability, trait mutation rate 10^{-8} , and the optima shift began at five generations after a $10N$ generation burnin. Across our GSS simulations, we see the expected selection response (Supplementary Material Figure S7).

Overall, we see the same qualitative results under Gaussian stabilizing selection with optima shifts as under exponential directional selection. Stronger directional selection, here determined

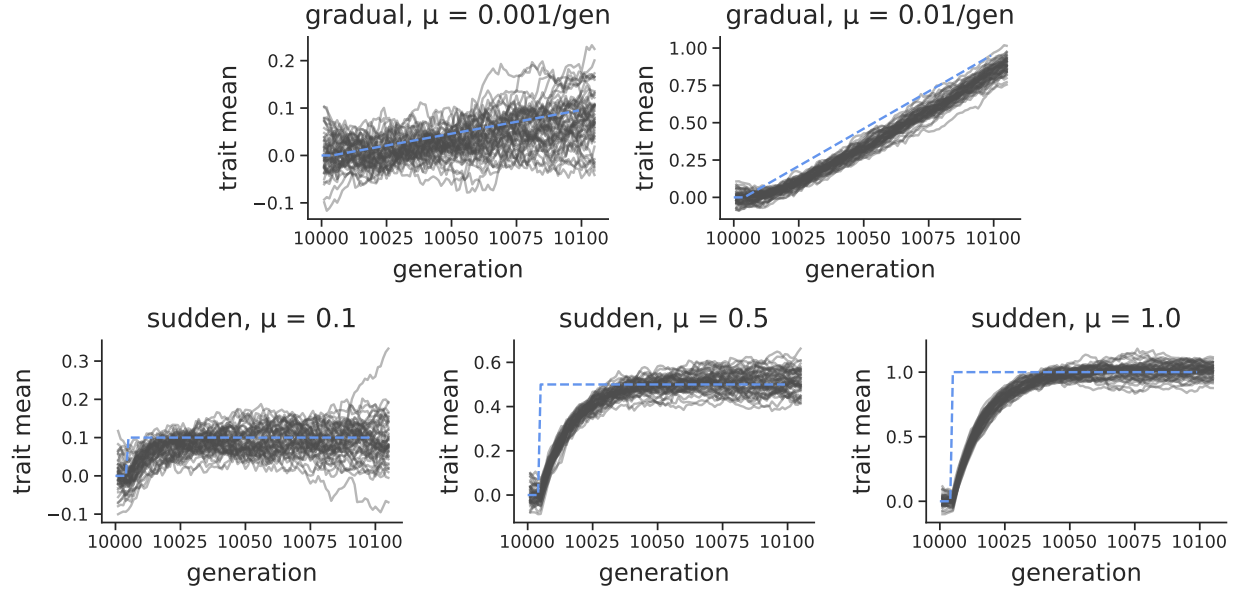


Figure S7: The population mean trait value under the Gaussian stabilizing selection simulations (gray lines) and the trait optima (dashed blue lines). The first row shows the selection response during a graduate shift in optima per generation, while the second row shows the selection response during a sudden optima shift.

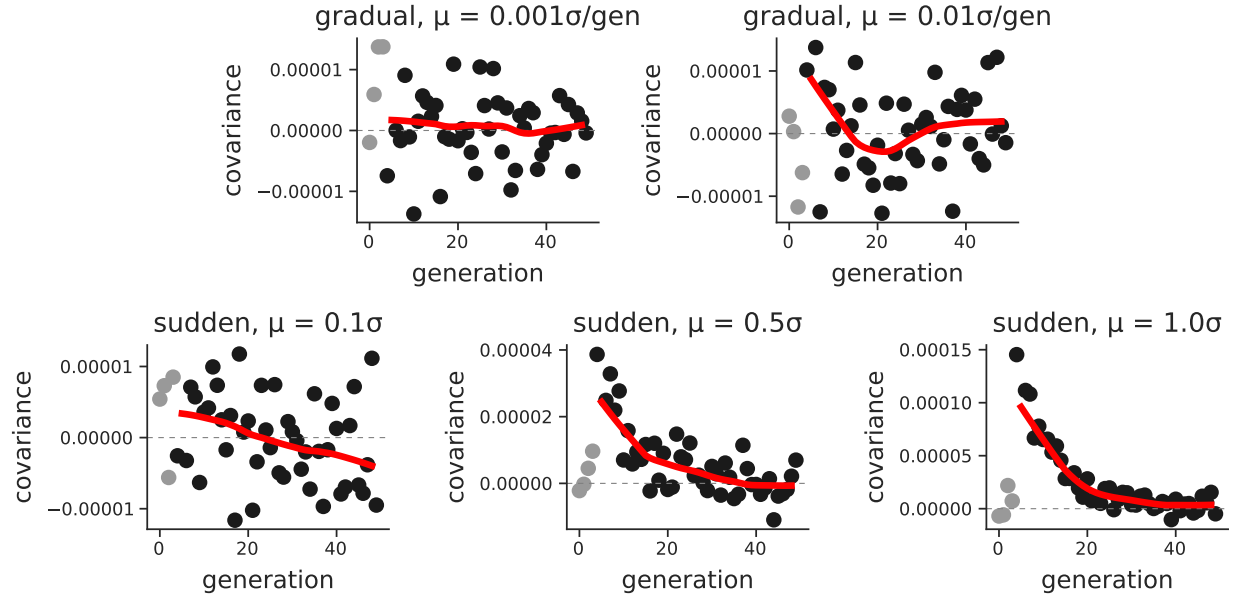


Figure S8: Mean temporal covariance ($\text{Cov}(\Delta p_5, \Delta p_t)$, with t varying across the x-axis) across 30 replicate simulations (light gray points are before the onset of selection; dark gray points are after selection begins), under different Gaussian stabilizing selection with optima shift regimes. The solid red line is a loess-smoothed average of these points.

by larger sudden optima shifts or larger gradual shifts per generation, lead to stronger temporal covariances (Supplementary Materials Figure S8). Furthermore, we see a stronger effect of linked selection, as measured by $G(t)$, under stronger directional selection (Supplementary Material Figure S9).

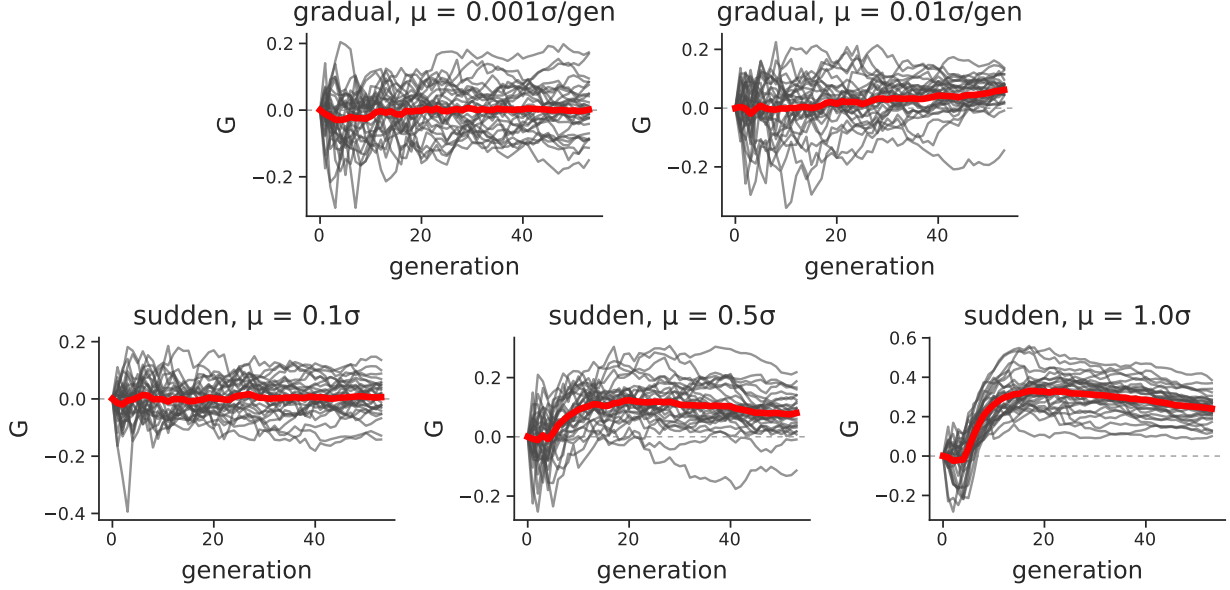


Figure S9: $G(t)$ trajectories across 30 replicate Gaussian stabilizing selection with optima shift regimes. The solid red line is a loess-smoothed average across replicates.

Additionally, we looked at the effect of the *replicate population size drawn from the same* population has on a single population’s $G(t)$ trajectories. These simulations had the same $10N$ generation burnin, followed by a change in population size emulating the bottlenecks associated with creating selection lines. Overall, we find that smaller population sizes lead to a reduced $G(t)$ (Supplementary Material Figure S10). This is expected, as the denominator of $G(t)$ is $\text{Var}(p_t - p_0)$, which has an inverse relationship with N_e ; as replicate population size is reduced, the proportion of allele frequency change driven by linked selection is lower, since the rate of drift is increased. To isolate the effects of varying replicate population size, we also looked at just the magnitude of temporal covariances (Supplementary Material Figure S11). We find that smaller replicate population sizes lead to *larger* temporal covariances. We then looked at the initial trait variance, which as expected, does not vary with replicate population size (since all burnin populations had the same size). This implies that the linkage disequilibria is higher in smaller populations, due to founder effects, which has the effect inflating the temporal covariance as predicted by our theory (Buffalo and Coop 2019).

S8.3 Convergence Correlations

Using the same exponential fitness function simulations described above, we also investigated how the convergence correlation is impacted by (1) genetic architecture, (2) the design of the selection experiment, e.g. how many individuals are selected for each line from the founding population, and (3) the direction of selection across the two populations “lines”. After burning in $N = 1000$ diploid populations for $10N$ generations, we simulated two equally-sized lines of sizes $n = \{50, 500, 1000\}$

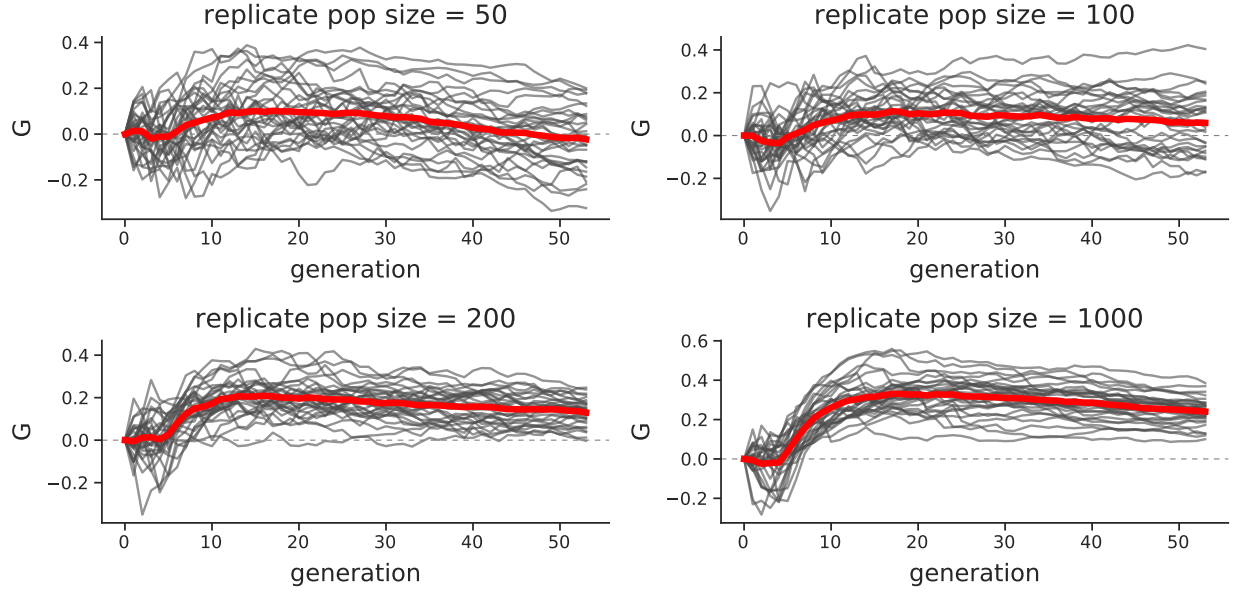


Figure S10: $G(t)$ trajectories under GSS after sudden optima shift of 1 at generation five, for varying replicate population sizes.

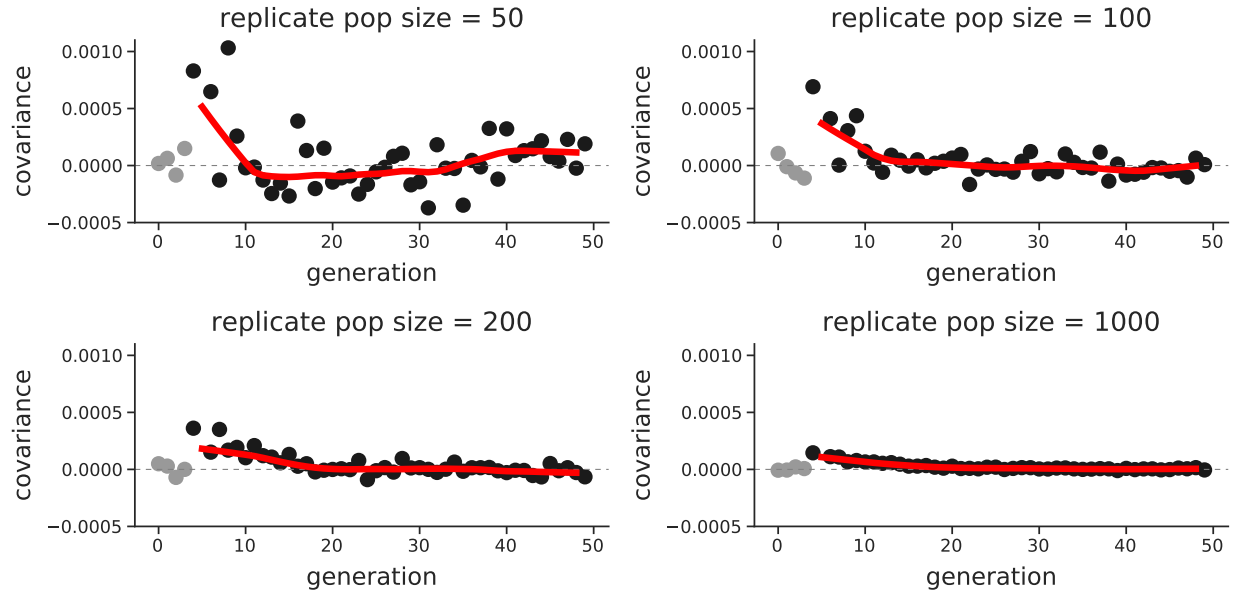


Figure S11: Temporal covariance $\text{Cov}(\Delta p_5, \Delta p_t)$, where t varies along the x-axis, for a sudden optima shift of 1, for varying replicate population sizes. The reference time point is the first generation of selection; dark gray points are the temporal covariance after selection began, and the light gray points are before.

diploids, and imposed three selection schemes across different simulation runs. First, we imposed a convergent selection scheme, where the populations undergo exponential directional selection in the same direction. We expect that the convergent correlation under this convergent scheme should

be positive, as the two lines should share some haplotypes carrying beneficial alleles, and these are selected in the same direction across the two lines. Second, we imposed divergent selection, where the two lines again undergo exponential directional selection, except in different directions. Here, we expect the convergence correlation to be negative, as haplotypes that increase the selected trait in one population are beneficial in the upward selected line, but deleterious in the downward selected line. Third, we have a control selection scheme, where one line is selected and the other is not; this is akin to the control line in the Castro et al. (2019) study (see Figure 2C). In this case, we expect to see no convergence correlation, as only one line is being selected. Finally, across these two-line simulation studies, we expect that smaller selection line sizes should show weaker convergent correlations, as the probability that the same haplotypes are selected between the two lines decreases with size.

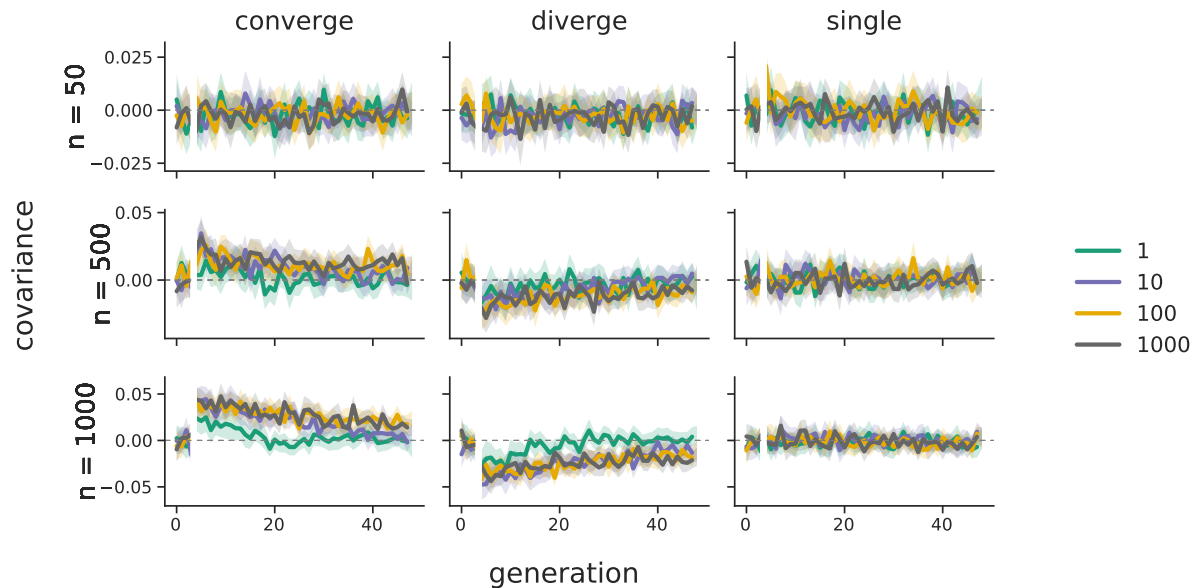


Figure S12: The convergence correlations across the two population line exponential directional selection simulations; panel rows are for differing line population sizes, and panel columns are the modes of selection across the lines (convergent, divergent, and only a single selected line control). Line color indicates the target genetic architecture, in number of loci affecting the trait’s value. 95% confidence intervals are also shown. Note that selection begins at generation five, which is the reference generation; this is indicated by the split in the lines.

Overall, our simulations confirm our hypotheses; see Supplementary Material Figure S12. We also find that in simulations *with* a monogenic genetic architecture (i.e. the target number of trait-affecting loci is $L = 1$), the convergence correlations are generally much weaker than those under a polygenic architecture. However, this effect is mediated by the line population size; the difference in convergence correlation between $L = 1$ and $L = 1000$ are more dissimilar when the line population sizes are larger (compare the first column, last two rows). Like the convergence correlations calculated on the Barghi et al. (2019) data, we find in simulations convergence correlations decay through time. Additionally, populations selected in opposite directions lead to negative convergence correlations, as expected. Overall, we find that the convergence correlation is affected by both genetic architecture and the size of the selected population lines.

We also wanted to test whether we see similar convergence correlations under Gaussian stabilizing selection. In these simulations, rather than targeting a particular V_A , we fix the trait mutation rate at 10^{-8} (thus region-wide $\theta = 2000$). Like the exponential directional selection simulations, we impose directional selection in the same direction across the two populations (converge), different directions (diverge), and only in one population (single). We also vary the type (gradual versus sudden) and magnitude of optima shifts in the two populations. Overall, simulations show convergence correlations for the sudden optima shifts in Supplementary Figure S13. Again, optima shifts in the opposite direction cause negative convergence correlations. We found that for slow moving optima shifts, the convergence correlations are generally too weak to be distinguished from zero reliably (*not shown*).

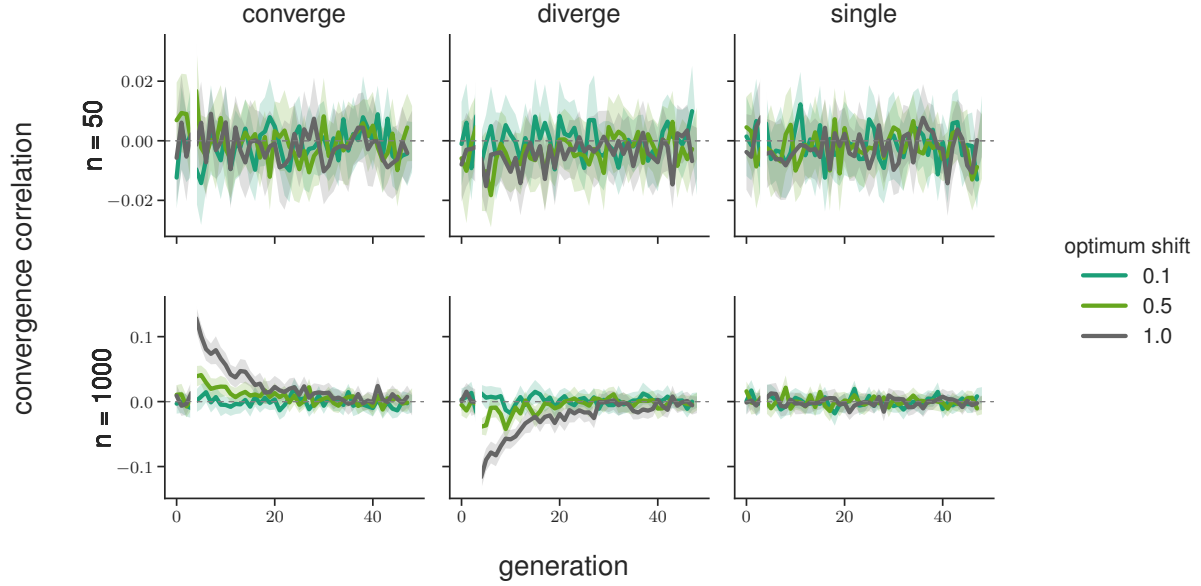


Figure S13: The convergence correlations across the two population line Gaussian stabilizing selection sudden optima shift simulations; selection line population sizes vary across rows, and panel columns are the modes of selection across the lines (convergent, divergent, and only a single selected line control). All simulations have a target number of loci affecting the trait of $L = 1000$; line color indicates the size of the sudden optima shift in standard deviations of V_S 95% confidence intervals are also shown. Note that selection begins at generation five, which is the reference generation; this is indicated by the split in the lines.

S8.4 Sampling in Temporal Blocks

In our analysis of the Barghi et al. (2019) data, we describe our statistic $G(t)$ as a lower bound for two reasons: (1) the population is sequenced every ten generations, meaning the temporal covariances between adjacent generations cannot contribute to the numerator of $G(t)$ but contributes to the denominator, and (2) the estimate of $G(t)$ ignores linked selection's contribution to the per-generation variance in allele frequency change. *In Buffalo and Coop (2019), we define an alternative estimator that includes selection's effects on these variance terms,*

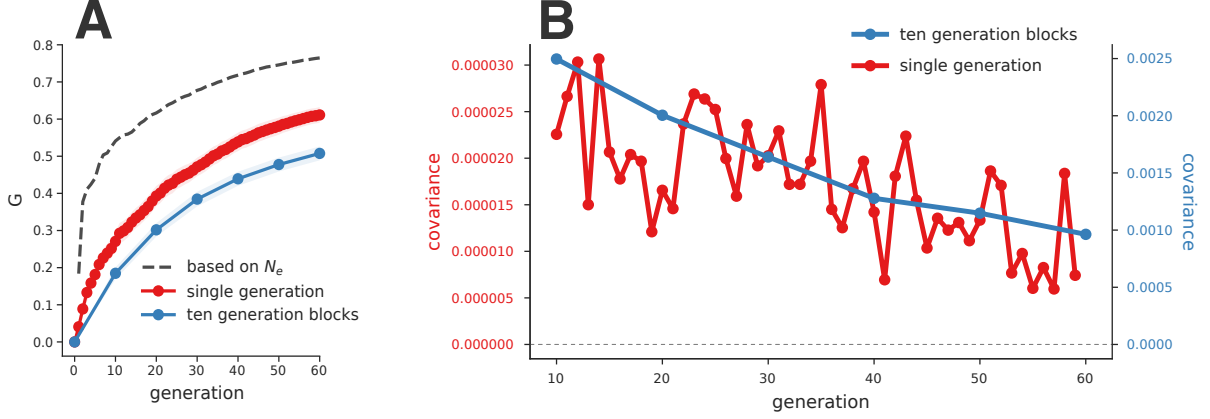


Figure S14: A: The $G(t)$ averaged over 50 replicate simulations with $V_A = 0.01$ and $L = 1000$. The blue line shows $G(t)$ calculated over ten generation blocks, similar to the calculation of temporal covariances of the Barghi et al. (2019) study. The red line shows the average $G(t)$ estimates when the population is sampled every generation and all covariances can contribute to the numerator of $G(t)$. The dashed *dark* gray line indicates the $G'(t)$ estimate, which uses the known drift effective population size of the simulations. B: The temporal covariances calculated each generation (red line) and on ten generation blocks (blue line) using the same simulation data.

$$G'(t) = 1 - \frac{t\mathbb{E}(p_0(1 - p_0))}{2N_e \text{Var}(p_t - p_0)}, \quad (\text{S56})$$

which can be calculated when the drift-effective population size N_e can be estimated (see equation 26 in Buffalo and Coop 2019 for details).

To verify that $G(t)$ estimated every ten generations is indeed a lower bound, we used a simulation procedure similar to the exponential fitness function simulations (described in Supplementary Material Section S8.1), and calculated the temporal covariances and $G(t)$ both each generation, and every ten generations. Unlike the simulations described in S8.1 *where selection began at $10N+5$ generations*, selection *starts at generation $10N$ here*, and used trait $V_A = 0.01$ and targeted $L = 1000$ sites affecting the trait.

First, comparing $G(t)$ when sampling population frequencies every generation versus every ten generations, we confirm that the ten-generation block $G(t)$ is a lower bound of the $G(t)$ trajectory when sampling is every generation (red and blue lines in Supplementary Figure S14A). Furthermore, since we control the population size *and reproductive sampling scheme* in our simulations at $N = 1000$ diploids, we know the drift-effective population size in the absence of selection, *which allows us to estimate $G'(t)$* . Plugging in the drift-effective population size $N_e = 1000$ into the expression for $G'(t)$ and using the $\text{Var}(p_t - p_0)$ calculated for different t 's, we see that $G(t)$ calculated every generation does not account for linked selection's inflation of $\text{Var}(\Delta p_t)$ and underestimates the true impact of linked selection as expected (dashed gray line in Supplementary Figure S14A).

To further understand the effects of calculating temporal covariances every ten generations rather than every generation, we also compared their magnitudes and decay rates using the simulations described above. We find that ten generation block temporal covariances are orders of magnitude larger but decay at similar rates (see Supplementary Figure S14B; note the two y-axis scales are different). The larger magnitude is expected, as each ten generation block temporal

covariance is the sum of 45 temporal covariances between adjacent generations (e.g. $\binom{10}{2}$).

S8.5 Background Selection

In our previous work, Buffalo and Coop (2019), we did not investigate whether background selection can lead to temporal autocovariance. Here, using forward-in-time simulations, we find that background selection can indeed generate temporal autocovariance and lead to convergence correlations when deleterious haplotypes are shared between populations and both are removed by selection.

We simulated background selection in a 50 megabase region, where deleterious alleles are randomly introduced by mutation. Following background selection literature (Charlesworth et al. 1993; Hudson and Kaplan 1995; Hudson and Kaplan 1994; Nordborg et al. 1996), we parameterize the mutation rate as the total number of deleterious mutations introduced per diploid genome, per generation, and simulate values $U = \{0.5, 1.0, 1.5\}$. Note that for our 50Mb region, our choice of BGS U parameters are on the higher end of the spectrum expected for *Drosophila*, but we wanted to ensure the strength was sufficient to see a signal. Note that if $U \approx 1.6$ (Elyashiv et al. 2016), and the *Drosophila* genome is $\approx 140\text{Mb}$, our region is $\approx 36\%$ of the genome; this implies a reasonable U for our region is $U \approx 0.57$, which is close to the bottom end of our parameter range. We also vary the strength of selection against the deleterious mutations, $s = \{0.01, 0.05, 0.1\}$, as well as different recombination rates ($r_{bp} = \{10^{-7}, 10^{-8}\}$). Like other simulations, we burnin the population for $10N$ generations under background selection. Overall, we find background selection does create temporal covariance (Supplementary Material Figure S16), which are stronger under (1) higher deleterious mutation rates and (2) larger selection coefficients. This latter point initially seems at odds with background selection theory, as the level of pairwise diversity in a region under strong background selection is invariant with respect to the selection coefficient. However, looking at the background selection $G(t)$ trajectories, we find that over time, background selection appears to trend towards an *asymptote* in the $r_{BP} = 10^{-7}$ subfigure, and reaches an equilibrium in the $r_{BP} = 10^{-8}$ subfigure that seems reasonably invariant to the choice of s (Supplementary Material Figure S15). We believe that these observations can be reconciled by $Cov(\Delta p_t, \Delta p_{t'})$ being larger for larger s when $|t' - t|$ is small, but also decaying more rapidly with $|t' - t|$, such that the overall contribution of selection to allele frequency variance is invariant to s (for strong background selection). However, further work is needed to fully explore and understand the temporal covariance dynamics of background selection.

Additionally, we investigated whether background selection can create convergence correlations between two replicate populations. Much like the exponential directional selection and Gaussian stabilizing selection simulations, we burned in a population for $10N$ generations with background selection, which continued after the population was split into two replicate populations. These simulations fixed $U = 1.0$, $r_{BP} = 10^{-8}$, and varied the replicate population size $n = \{200, 1000\}$. We find that background selection can create convergence correlations (Supplementary Material Figure S17). We find the convergence correlation is weaker in smaller replicate population sizes, as there are fewer shared haplotypes carrying the same deleterious alleles between the two populations.

Finally, we found in *processing these background selection simulation results* that including or excluding sites fixed or lost through time can lead to differences in the estimated $G(t)$ trajectories and temporal covariance. We discuss this extensively in a subsequent section, Supplementary Materials Section S8.7.

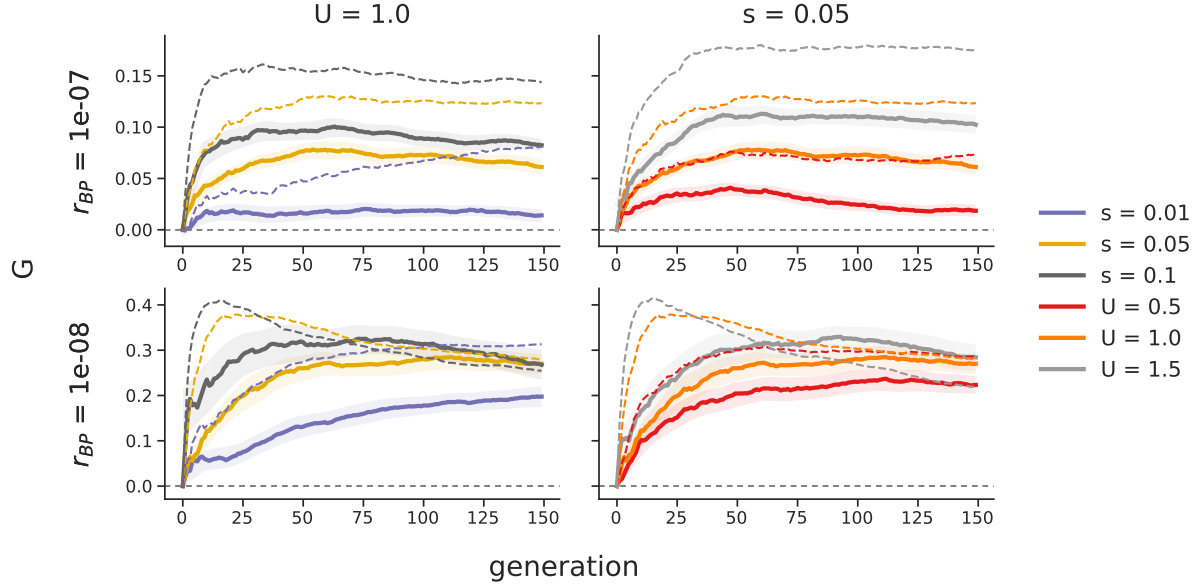


Figure S15: The trajectories of $G(t)$ through time under background selection, under different recombination rates (r_{BP} , rows), selection coefficients (s), and deleterious mutation rates (U). The first column *fixes* $U = 1.0$, and s varies, while in the second column $s = 0.05$ is held constant, and U varies. $G(t)$ is calculated using both including fixed sites (solid lines) and not including fixed sites (dashed lines).

S8.6 Truncation Selection

We also explored how directional truncation selection generates temporal covariances. In these simulations we select the top 10%, 25%, or 50% of the phenotypic distribution of individuals to form the next generation. We burnin these simulations using a neutral burnin routine, where trait alleles are selectively neutral until directional selection is imposed. More extreme directional truncation selection generated larger initial covariances (Supplementary Material Figure S18B). However, weaker truncation selection generated more sustained positive covariances and so *have* a larger long-term impact on the variance in allele frequency change. We again noticed fixation or loss of sites has a strong effect on temporal covariance and $G(t)$ under truncation selection. Here, since only a (potentially small) fraction of individuals contribute to the next generation, sites can fix over very short timescales. Furthermore, the small number of effective breeders contributing to the next generation shrinks N_e considerably, which increases $\text{Var}(p_t - p_0)$, the denominator of $G(t)$. We see both the effect of handling fixed/lost sites differently and the faster rate of drift in Supplementary Materials Figure S18A, where weaker truncation selection actually has higher levels of $G(t)$. Looking just at temporal covariances, we find that stronger truncation selection (e.g. a smaller tail of individuals selected) does lead to greater temporal covariances. Overall, these truncation selection simulations demonstrate the value of considering both absolute measures of selection's effect on allele frequency changes, i.e. temporal covariance, as well as measures relative to drift, i.e. the $G(t)$ trajectories. While selecting a smaller tail of individuals is associated with *stronger* selection, it also is leading to a faster rate of drift, which can distort conclusions inferred from considering the $G(t)$ trajectories alone.

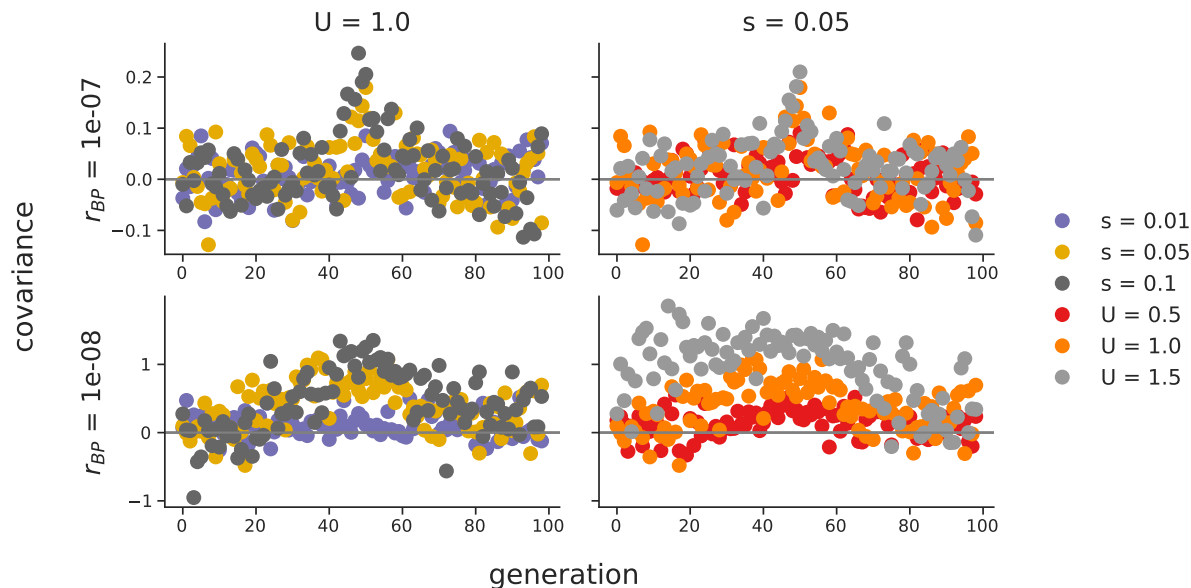


Figure S16: The temporal covariances, $\text{Cov}(\Delta p_{50}, \Delta p_t)$ (where t varies along the x-axis) created by background selection, under different recombination rates (r_{BP} , rows), selection coefficients (s), and deleterious mutation rates (U). Unlike directional selection figures, where we choose the reference generation to be the first generation after the onset of selection, here we choose an arbitrary reference generation (generation 50). The symmetry of temporal covariance around the reference generation, is expected, since unlike directional selection the level of additive genetic variance for fitness has hit mutation-selection-drift balance. Note that the first column sets constant $U = 1.0$, and s varies, while the second column sets $s = 0.05$ constant, and varies U .

S8.7 The Effect of Fixations in the Empirical Datasets

In our simulation results, we noticed the temporal covariances and $G(t)$ statistics can differ depending on how allele frequencies of zero or one are handled. Generally, temporal covariances should be calculated on polymorphic sites; once a site has reached fixation or loss, its allele frequency change $\Delta p_t = 0$ and including these sites in the temporal covariance calculation can lead to biases. However, with *sample* allele frequencies, rather than population frequencies, a site with observed frequency zero or one may still be segregating, but by chance not sampled at a timepoint. Here, we discuss the effect of including sites with frequency zero or one, and show our empirical results are not qualitatively different when analyzed excluding fixed sites.

With empirical data calculated on sample allele frequencies, low frequency minor alleles may not be sampled at some timepoints, and excluding these observations (instead of treating it as a trajectory that has a 0 frequency timepoint) biases estimates of quantities such as N_e towards intermediate frequency alleles. Additionally, we tried only dropping fixed or loss sites from the temporal covariance calculations that were at the end or the beginning of a trajectory (e.g., as if the site was created by a new mutation or fixed); while this ameliorated some of this bias it did not remove all of it. Overall, we found by trying all these approaches that not removing fixed or lost sites was the best way to deal with sample allele frequencies that could be missing from some timepoints.

To ensure that our findings were robust to handling sites with a frequency of zero or one differ-

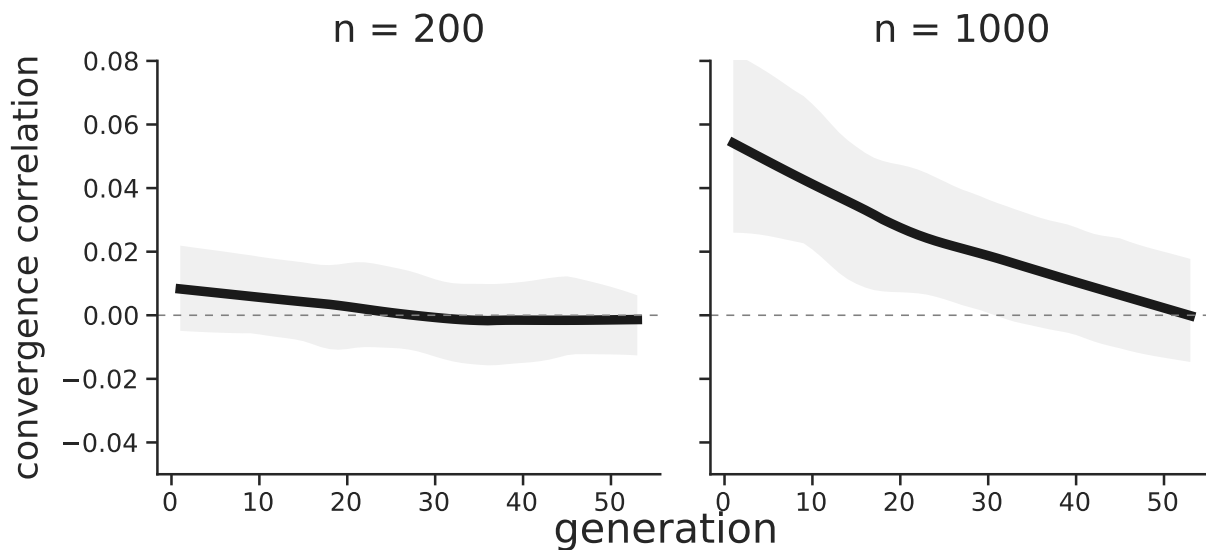


Figure S17: The convergence correlation created by background selection through time, since the population split. The replicate population size varies between the two panels. Values are averaged over 30 replicate simulations, while the interval is a 95% confidence interval.

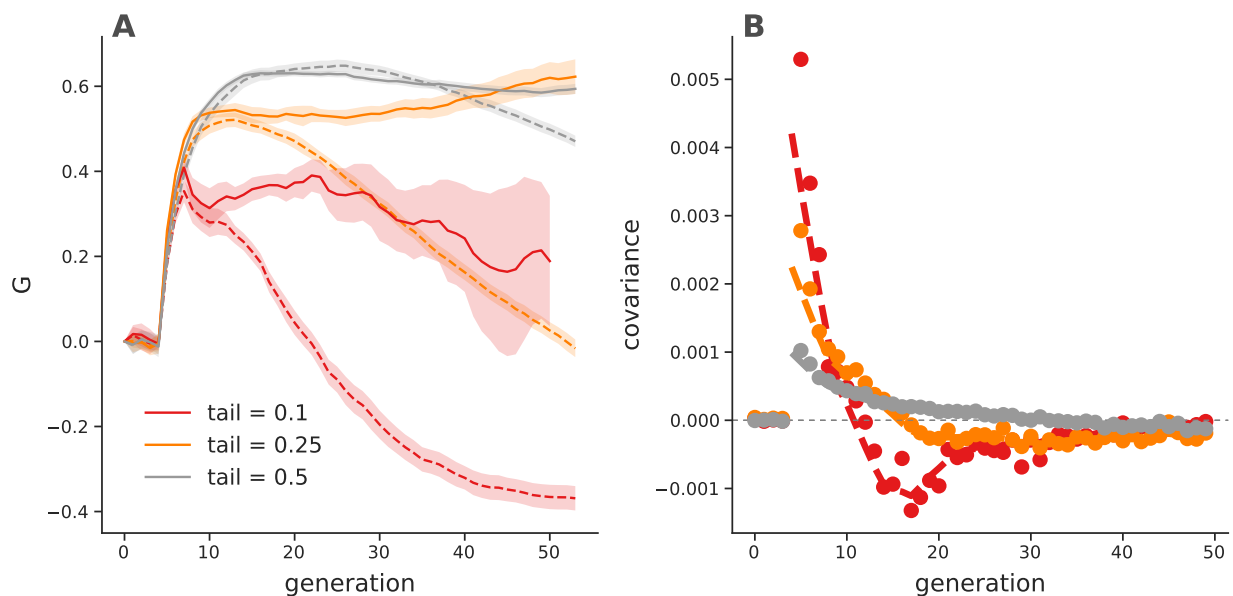


Figure S18: $G(t)$ trajectories (A) and temporal covariances (B) from truncation selection simulations for different numbers of individuals selected (line color). Dashed lines indicate $G(t)$ trajectories and temporal covariances calculated *including* fixed sites, while the solid lines exclude fixed sites. All values are averaged over 30 replicate simulations; the lines in the right figure are loess smoothed, while points are averages. The solid lines of the temporal covariances have been excluded in the left figure for clarity, but are similar except they do not become negative.

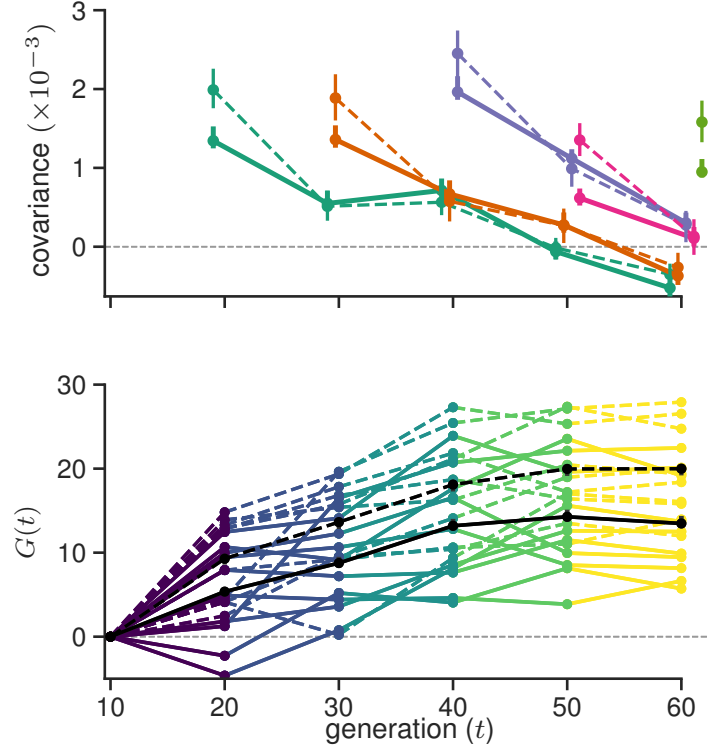


Figure S19: The effect of excluding fixed/lost sites in the calculation of the temporal covariances and $G(t)$ trajectories of the Barghi et al. (2019) data. Dashed lines are those including fixed/lost sites (i.e. the original Figure 1), and solid lines are excluding fixed/lost sites.

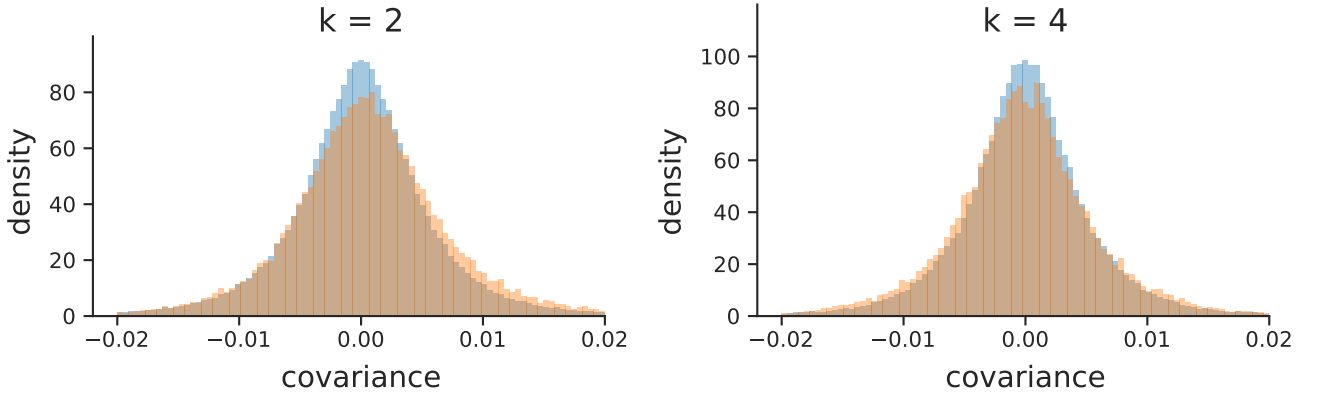


Figure S20: A version of Figure 3 (A) and (B) excluding fixed and lost sites. The same qualitative pattern holds as the original figure, which did not exclude fixed and lost sites: there is an enrichment of positive temporal covariances between near timepoints ($k=2$) in the Barghi et al. (2019) study, and an excess of negative temporal covariances at more distant timepoints ($k=2$).

ently, we regenerated Figures 1 and Figure 3 but excluded frequencies of zero or one. Specifically, we wanted to ensure that our finding that temporal covariances were negative at later timepoints

was not spuriously caused by the way fixed or lost sites are handled. We see no qualitative difference (Supplementary Material Figures S19 and S20) that emerges when sites with frequency zero or one are excluded.

S9 Additional Figures

S9.1 PCA of Barghi et al. (2019) replicates

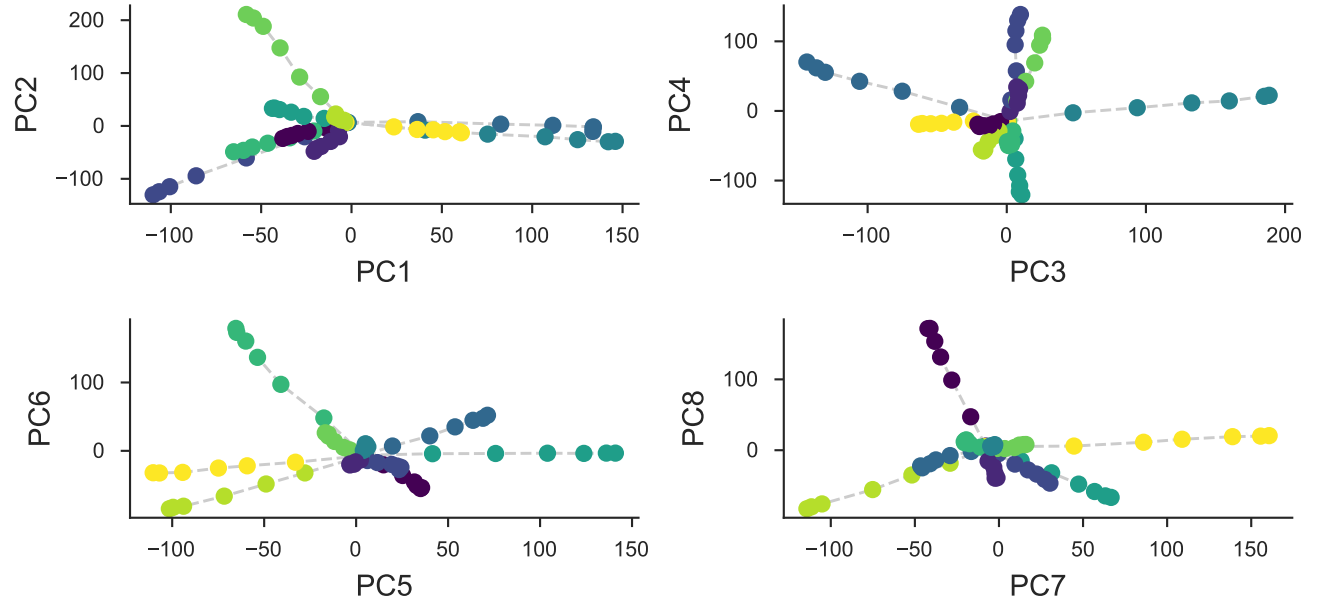


Figure S21: A PCA on the centered and standardized population frequencies for each replicate (each color) for all its sequenced timepoints (the connected series of points). All replicates start from the same source population, and thus are overlapping in the center; as each replicate evolves independently it diverges from the other replicates in PCA space.

S9.2 Bias Correction for Barghi et al. (2019)

We have investigated the effectiveness of our correction on real data by exploiting the relationship between sampling depth and the magnitude of the variance and covariance biases, and comparing the observed variances and covariances before and after correction. We plot the variance and covariance (between adjacent time intervals) before and after the bias correction against the average sample depth in 100kb genomic windows in Figure S22. Overall, we find the biased-correction procedure removes the relationship between variance and covariance and depth, indicating it is working adequately.

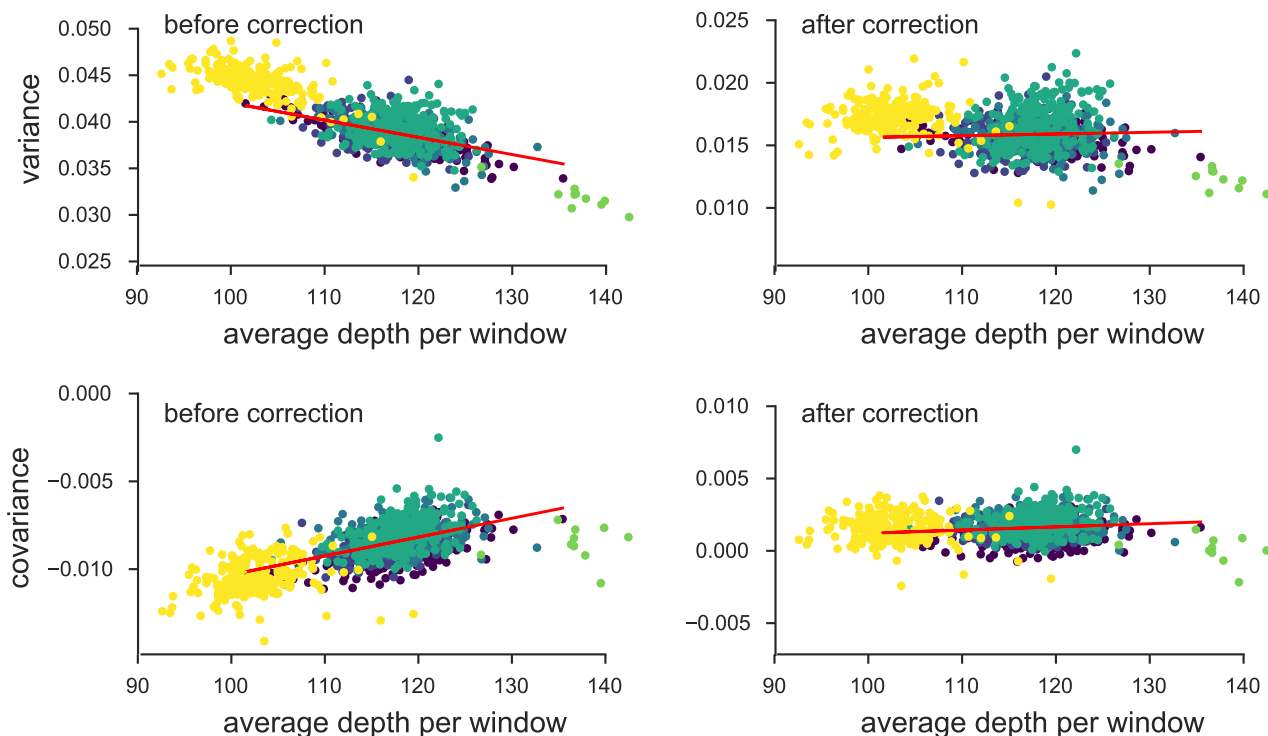


Figure S22: The variance and covariances from the Barghi et al. (2019) study, calculated in 100kb genomic windows plotted against average depth in a window before and after bias correction. Each panel has a least-squares estimate between the variance and covariance, and the average depth. Overall, the bias correction corrects sampling bias in both the variance and covariance such that the relationship with depth is constant. Colors indicate the different chromosomes of *D. simulans*; we have excluded the X chromosome (yellow points) and chromosome 4 points (green points to far right) from the regression due to large differences in average coverage.

S9.3 Barghi et al. (2019) Temporal Covariances Per Replicate

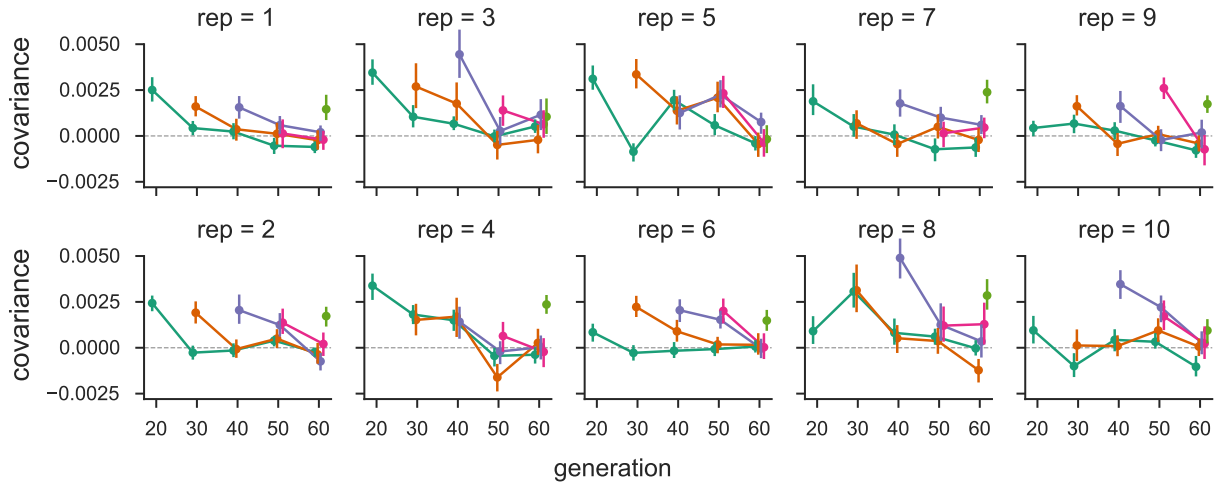


Figure S23: The temporal covariances from the Barghi et al. (2019) study, for each replicate individually. As in Figure 1, each line follows the temporal covariances from some initial reference generation through time, which represent the rows of temporal covariance matrix.

| s | t | median | median 95% CI | trimmed mean | trimmed mean 95% CI |
|----|----|--------|------------------|--------------|---------------------|
| 0 | 10 | 1.629 | [1.532, 1.738] | 1.874 | [1.777, 1.969] |
| 0 | 20 | 0.371 | [0.276, 0.465] | 0.491 | [0.403, 0.585] |
| 0 | 30 | 0.479 | [0.4, 0.589] | 0.516 | [0.434, 0.602] |
| 0 | 40 | 0.059 | [-0.012, 0.15] | 0.027 | [-0.05, 0.099] |
| 0 | 50 | -0.204 | [-0.271, -0.125] | -0.259 | [-0.329, -0.187] |
| 10 | 20 | 1.549 | [1.427, 1.659] | 1.722 | [1.617, 1.83] |
| 10 | 30 | 0.438 | [0.339, 0.539] | 0.506 | [0.399, 0.609] |
| 10 | 40 | 0.233 | [0.149, 0.328] | 0.254 | [0.159, 0.343] |
| 10 | 50 | -0.355 | [-0.454, -0.289] | -0.319 | [-0.401, -0.237] |
| 20 | 30 | 1.981 | [1.856, 2.095] | 2.195 | [2.084, 2.302] |
| 20 | 40 | 0.792 | [0.698, 0.894] | 0.903 | [0.815, 0.999] |
| 20 | 50 | 0.123 | [0.042, 0.207] | 0.221 | [0.141, 0.309] |
| 30 | 40 | 1.296 | [1.208, 1.425] | 1.385 | [1.287, 1.483] |
| 30 | 50 | 0.07 | [-0.037, 0.183] | 0.116 | [0.023, 0.21] |
| 40 | 50 | 1.36 | [1.271, 1.446] | 1.513 | [1.427, 1.601] |

Table S1: Table of median of windowed covariance estimates ($\text{Cov}(\Delta p_s, \Delta p_t) \times 100$) between generations t and s and the trimmed mean windowed covariance which excludes the lower and upper 5% windows with the highest covariance.

S9.4 Barghi et al. (2019) Trimmed Window Covariances

Here we report median and trimmed mean of the windowed covariances (Supplementary Table S1). We note that the median covariance is also limiting result of a trimmed mean that symmetrically excludes the upper and lower α tails to calculate the trimmed average windowed covariance. As α increases to 0.5, the trimmed covariance converges to the median windowed covariance (by the definition of the median; see Supplementary Figure S24). Thus our genomic temporal covariances are non-zero due to the impact of selection on many genomic windows.

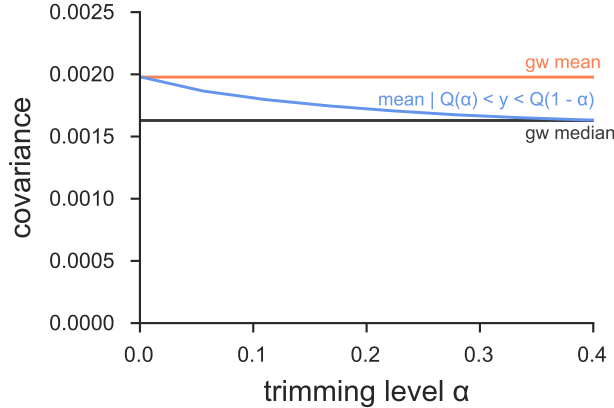


Figure S24: The genome-wide covariance ($\text{Cov}(\Delta p_0, \Delta p_{10})$ pooling all replicates) averaged (red line) and the median windowed covariance (blue) for the Barghi et al. (2019) dataset. The trimmed average window covariance, excluding the α lower and upper tails, converges to the median windowed covariance. This indicates that genome-wide covariances are not being overly dominated by a large-effect loci in few windows.

S9.5 Barghi et al. (2019) Empirical Null and Windowed Covariance Distributions

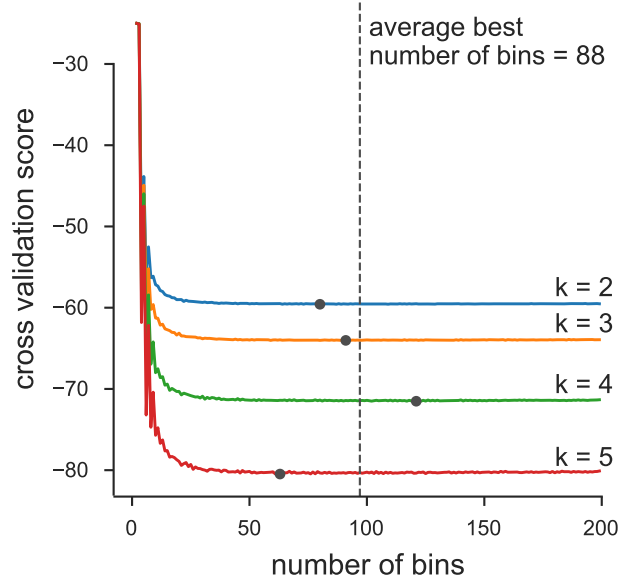


Figure S25: We chose number of bins used in the histograms of Figure 3 via an analytic expression for the cross-validation risk, based on the equation 6.16 of (Wasserman 2006, p. 129). Above, we plot the cross-validation risk for various numbers of bins, for each of the four off-diagonals of the temporal covariance matrix that we analyze. Overall, because the number of data points is large, oversmoothing is less of a problem, leading the cross-validation risk to be relatively flat across a large number of bins. Each gray point indicates the minimal risk for a particular off-diagonal, and the dashed line indicates the best average binwidth across off-diagonals.

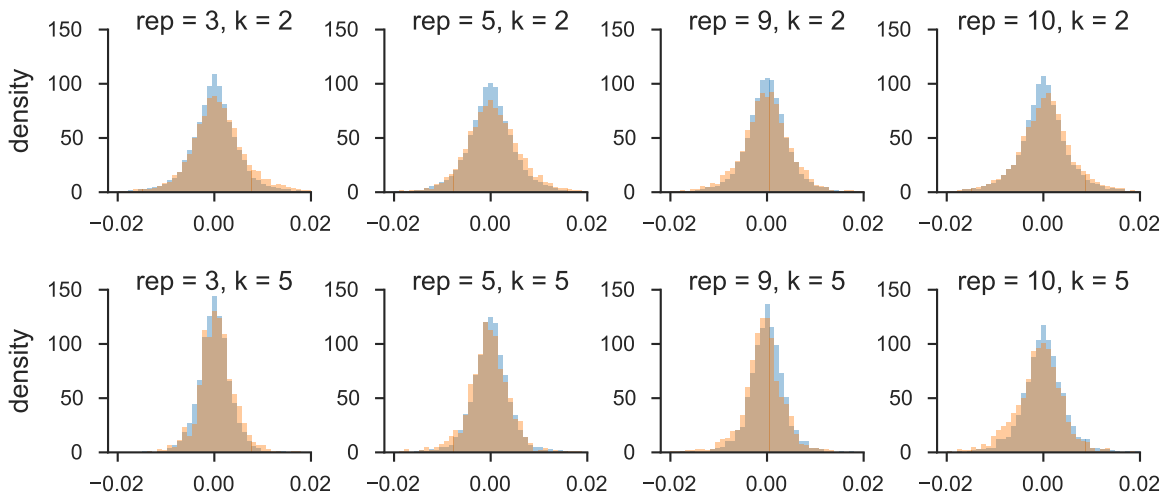


Figure S26: The distribution of windowed temporal covariances alongside the empirical neutral null for five randomly sampled replicates (columns), for $k = 2$ (first row) and $k = 5$ (second row). The main figure of the paper pools all replicate window and empirical neutral null covariances; we show here the windowed temporal covariances tend to shift from being positive (a heavier right tail) to become more negative (a heavier left tail) through time within particular replicates.

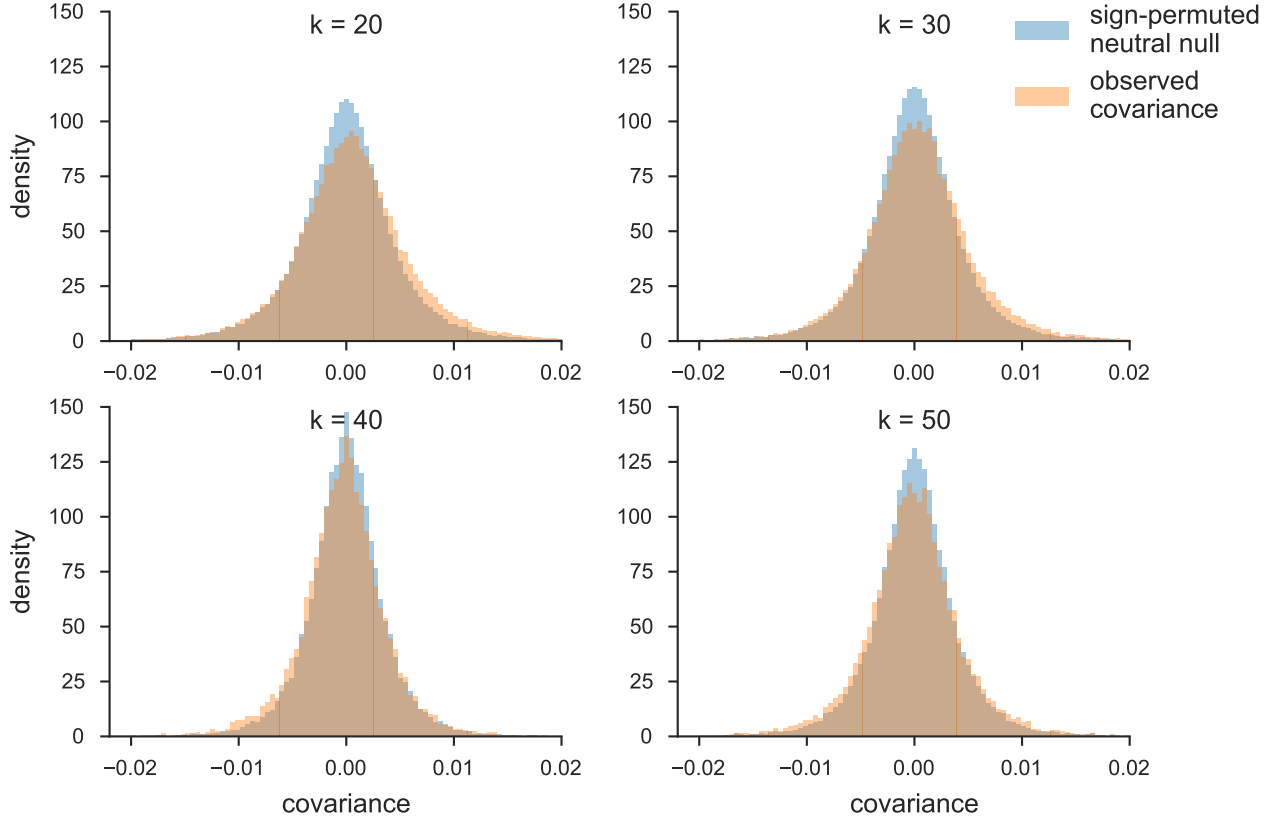


Figure S27: The distribution of temporal covariances calculated across 100kb genomic windows from Barghi et al. (2019)’s study (orange) and the block sign permuted empirical neutral null distribution of the windowed covariances (blue). Each panel shows these windowed covariances and the empirical null distribution for covariances $\text{Cov}(\Delta p_t, \Delta p_{t+k})$, k is the number of generations between allele frequency changes.

S9.6 Barghi et al. (2019) Tail Probabilities for Windowed Covariances Distributions

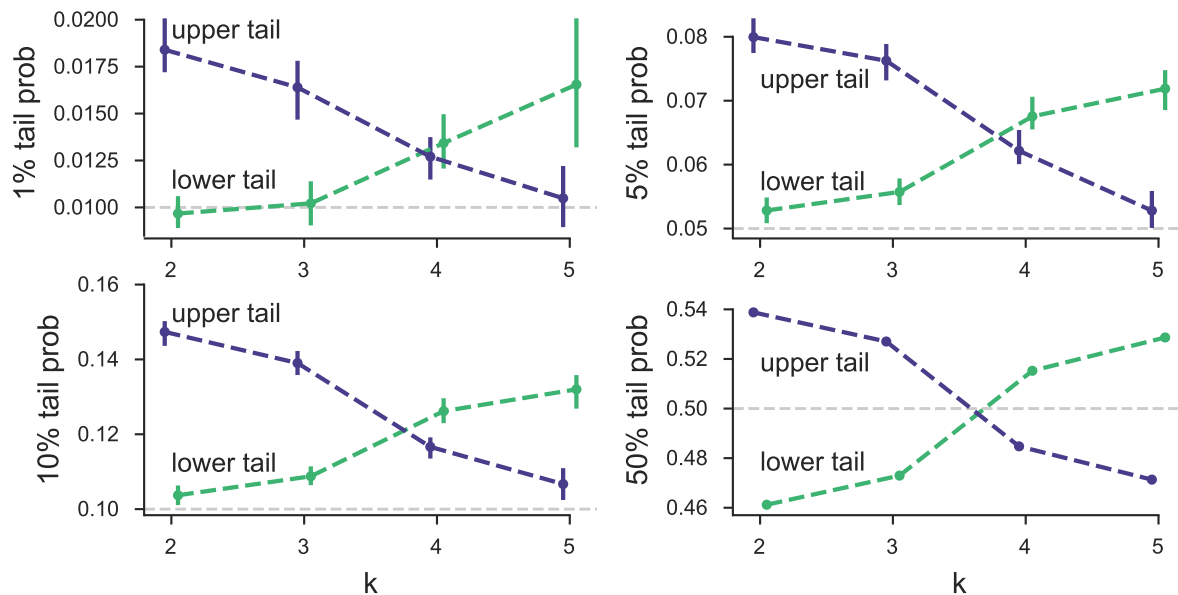


Figure S28: Barghi et al. (2019) tail probabilities compared to sign-permuted empirical null distribution for various α levels.

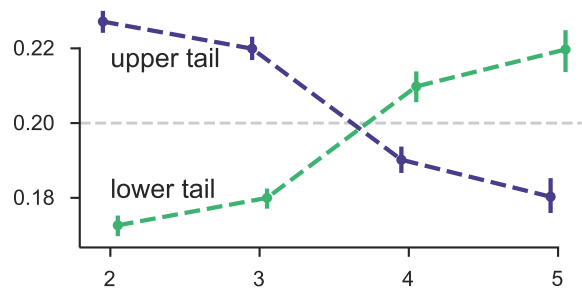


Figure S29: The 20% lower and upper tail probabilities for the observed windowed covariances from the Barghi et al. (2019) study, based on sign-permuting at the chromosome level. This permutation empirical null is robust to long-range linkage disequilibrium acting over entire chromosomes (see Supplementary Material section S5).